Long-term evolution of the West African Transform margin : estimates of denudation from Benin using apatite thermochronology

Mark M Wildman, David Mark Webster, Roderick Brown, Dominique Chardon, Delphine Rouby, Jing Ye, Damien Huyghe, Massimo Dall'asta

To cite this version:

Mark M Wildman, David Mark Webster, Roderick Brown, Dominique Chardon, Delphine Rouby, et al.. Long-term evolution of the West African Transform margin : estimates of denudation from Benin using apatite thermochronology. Journal of the Geological Society, 2019, 176 (1), pp.97-114. 10.1144/jgs2018-078 . insu-01875318

HAL Id: insu-01875318

https://insu.hal.science/insu-01875318v1

Submitted on 17 Sep 2018

Accepted Manuscript

Journal of the Geological Society

Long-term evolution of the West African Transform margin: Estimates of denudation from Benin using apatite thermochronology.

Mark Wildman, David Mark Webster, Roderick Brown, Dominique Chardon, Delphine Rouby, Jing Ye, Damien Huyghe & Massimo Dall'Asta

DOI: https://doi.org/10.1144/jgs2018-078

Received 10 April 2018
Revised 29 August 2018
Accepted 30 August 2018

Supplementary material at https://doi.org/10.6084/m9.figshare.c.4220804

To cite this article, please follow the guidance at http://www.geolsoc.org.uk/onlinefirst#cit_journal

Long-term evolution of the West African Transform margin: Estimates of denudation from Benin using apatite thermochronology.

Wildman, M. [1,2], Webster, D. [1], Brown, R. [1], Chardon, D. [3], Rouby, D. [3], Ye, J. [3], Huyghe, D. [3], Dall'Asta, M.[4]

1. School of Geographical and Earth Sciences, College of Science and Engineering, University of Glasgow, Gregory Building, Glasgow, G12 8QQ, Scotland.

2. Géosciences Rennes, Université de Rennes 1, Rennes, 35042, France.

3. GET, Université de Toulouse, CNRS, IRD, UPS, Toulouse, France.

4. Total R&D, CSTJF Av. Larribau- 64018 Pau Cedex –France

Abstract

The Benin continental margin was formed during the breakup of Gondwana through oblique rifting along transform faults. The evolution of topography following breakup directly impacts the evolution of sedimentary basins, which has major implications for hydrocarbon exploration in the region. Quantitative constraints on erosion across Benin are limited to the Cenozoic, based on analysis of dissected lateritic paleolandscapes. To resolve the Mesozoic erosion history, we have obtained apatite fission track and single-grain (U-Th-Sm)/He data from 18 samples collected across a 600-km-long transect through Benin. We invert these data, including available geological and geomorphic constraints, to obtain time-temperature paths, which are used to estimate magnitudes of denudation over the last 200 Myr. Our study suggests denudation was focussed over a c. 300-km-long seaward sloping limb of the marginal upwarp and at the southern margin of the interior Iullemmeden Basin from 140-100 Ma with lower magnitudes of denudation characterising the continental interior and post-Cretaceous evolution of the margin. Models are consistent with modest burial (c. 1 km) of the Iullemmeden Basin between 120 and 85 Ma, and of the continental margin between 85 and 45 Ma. By the Eocene, the first-order relief of Benin had developed with regional erosion rates <20m/Myr since then.

Supplementary information: Supplementary information includes radial plots for single grain AFT ages; information on stratigraphic and geomorphological constraints for thermal history models; plots of apatite (U-Th-Sm)/He ages against eU and crystal size; data predictions for maximum likelihood and posterior thermal history models; graphics of the log likelihood and number of time-temperature points for model runs; full details on the modelling input; details on geological and geomorphological constraints; and further data on denudation/burial magnitudes and rates.

Transform margins are associated with significant strike-slip movement during continental breakup that results in structural and thermal histories distinct from purely divergent rifted margins (Edwards *et al.*, 1997; Guiraud *et al.*, 2010). Zones of normal rifting in the central and equatorial Atlantic are segmented by large fracture zones where movement along transform faults offset the West African Central and Equatorial mid-Atlantic ridge (Fig. 1a) that segment (Bonatti, 1996).

Diachronous normal divergence opened the Central Atlantic Ocean from south to north, beginning in the Early to Middle Jurassic (200 to 185 Ma) (e.g., Withjack *et al.*, 1998; Labails *et al.*, 2010) forming rifts inland and along the future continental margins, which branch into future Guinea-Liberia margin segment of the Equatorial Atlantic (Fig. 1a). The onset of rifting in the Central Atlantic at 200 Ma was synchronous with the emplacement of the Central Atlantic Magmatic Province (CAMP, Fig. 1a); however, the relationship between CAMP magmatism and continental breakup is still debated (Leleu *et al.*, 2016). During the Early Cretaceous rifting propagated northward from the southern Atlantic due counterclockwise rotation of the African plate (Moulin *et al.*, 2009). From the late Barremian to late Albian (c. 125─100 Ma), extension occurred along a series of rifts and major transform faults experienced dextral movement. Movement along these transform faults propagated westward to open the Equatorial Atlantic Transform margin (Fig. 1a) and triggered lithospheric breakup in the late Albian (Nemčok *et al.*, 2013; Heine and Brune, 2014; see Ye *et al.*, 2017 for a review).

The potential hydrocarbon reservoirs of the West-African offshore basins have received much attention from geophysics and seismic studies to reveal the basin crustal architecture and stratigraphy (Brownfield & Charpentier, 2006; Nemčok *et al.*, 2013; Ceraldi *et al.*, 2017 and references therein), whereas the timing and magnitude of erosion and burial across the onshore domain over 10─100 Myr timescales remains poorly understood. The present-day Benin transform margin is characterised by a low-elevation marginal upwarp (Fig. 1b, Fig. 2a); however, during rifting, topography may have been created where transform faults segmented divergent margins, with escarpments forming towards the transform valley and gentle slopes away from the fault (Basile & Allemand, 2002). Obtaining constraints on long-term erosion and burial is an important step in understanding (i) the evolution of pre-, syn and post-rift topography, (ii) the response of regional drainage networks, and (iii) the partitioning of sedimentary fluxes between offshore or intracontinental basins.

Dissected laterite-capped paleolandscapes preserved across West Africa have been used to determine that the rate of denudation has been extremely low since the Eocene (c. 2─20 m/Myr and mostly < 10 m/Myr, Beauvais *et al.*, 2008; Beauvais & Chardon, 2013; Grimaud *et al.*, 2014, 2015, 2018). The earlier history of erosion and landscape evolution across the West African margin remains unresolved. Low-temperature thermochronology is ideally suited to fill this knowledge gap by providing information on the timing and rate of cooling and heating of rocks as they pass through the upper crust. Using apatite fission track (AFT) and (U-Th-Sm)/He (AHe) thermochronology data, we investigate the thermal history of a 600-km-long, approximately coast-perpendicular, transect across the Benin marginal upwarp between the interior Iullemmeden Basin and the coastal basin. By obtaining thermal history information using a Bayesian inverse modelling approach and incorporating known geomorphological constraints we achieve new insights into the denudation and burial history of the continental margin over the past 200 Myr and into the partitioning of sedimentary fluxes across the margin.

Geological Setting of Benin

Regional geology

The geology of central Benin (Fig. 1a, Fig. 2b) consists of a Paleoproterozoic basement and Neoproterozoic sedimentary cover that were both involved in the late Neoproterozoic to earliest Paleozoic (i.e., Pan-African) Dahomeyides orogeny. Benin basement rocks are mostly amphibolite to granulite facies orthogneisses, some of which being migmatitic (Attoh *et al.*, 2013; Glodji *et al.*, 2014).

The Dahomey Belt (Fig. 2b) is made up of west-verging thrust-bounded structural units comprising metasedimentary rocks and gneisses (Ganade *et al.*, 2016). The Dahomey Belt is thrust over the Volta Basin, which is exposed in the northwest of Benin and comprises of sedimentary sequences deposited in a foreland setting during the Neoproterozoic to Cambrian (Deynoux *et al.*, 2006). The belt marks the collisional boundary between the West African Craton and the Nigerian shield (Kalsbeek *et al.*, 2012; Glodji *et al.*, 2014; Ganade *et al.*, 2016) (Fig. 1a, Fig. 2b). Pan-African, fold-and-thrust belts that developed around cratonic regions in northern South America and West Africa, such as the Dahomey Belt, were also associated with strike-slip movement during Phanerozoic times. The Dahomey Belt's structural inheritance influenced the development of fracture zones in the Equatorial Atlantic such as the central African fracture zone and Kandi Shear Zone (Basile *et al.*, 2005).

The Kandi Shear Zone (defined by the Kandi Fault, Fig. 2b) is a coast-perpendicular, N-S trending shear zone through central Benin. The Kandi Shear Zone developed during Pan-African continental collision and is proposed to be part of a transcontinental shear zone that extends into NE Brazil as the Transbrasiliano Lineament (Cordani *et al.*, 2013). Tectonic reactivation along both the

Transbrasiliano and Kandi lineaments has been reported to have occurred during the Paleozoic and Mesozoic (Guiraud & Alidou, 1981; Brito Neves & Fuck, 2014) and Cenozoic and recent tectonic activity proposed along the Transbrasiliano Lineament (Soares *et al.*, 1998; Barros *et al.*, 2015). Offshore, the Kandi Fault branches into the Romanche transform fault, which experienced phases of transpression through the Late Cretaceous and into the Neogene and is associated with the growth of transform-controlled anticlines (Basile *et al.*, 2005, Nemčok *et al.*, 2013; Ye *et al.*, 2017). Movement on the Kandi Fault can be seen in the offset of Cretaceous sediments in the Kandi Basin (Fig. 1a, Fig. 2b) (Guiraud, 1981) and has been observed in brittle microfaults and synkinematic quartz recrystallisations (Konate *et al.*, 2003).

The Iullemmeden Basin contains Paleozoic to Cenozoic sequences and covers an area of 7x10^5 km^2 extending from northern Benin to southern Algeria (Fig. 1a). A small sub-basin of the Iullemmeden Basin, the Kandi Basin, is approximately 160 km long and 45–95 km wide and is observed in north-eastern Benin and southern Niger (Fig. 2b). The Kandi Basin is bounded on the west by the Kandi Fault and consists of Cambro-Ordovician conglomerates and sandstones and a thin deposit of early Silurian siltstones (Alidou *et al.*, 1991; Konaté *et al.*, 2003). Unconformably overlying the Paleozoic units are (1) continental Lower Cretaceous siltstones and sandstones, (2) marine Upper Cretaceous shales, (3) Paleocene to early Eocene marine carbonates, and (4) late Eocene-early Oligocene fluvial sediments of the 'Continental Terminal' (Lang *et al.*, 1990; Konaté *et al.*, 2003; Chardon *et al.*, 2016; Fig. 1a, Fig. 2b).

The Benin Coastal Basin (Fig. 1a, Fig. 2b) is part of the Dahomey Embayment, which extends from Togo to western Nigeria (Brownfield & Charpentier, 2006). The Benin Coastal Basin reaches c. 100 km inland from the coast and overlies the basement rocks on the seaward sloping limb of the marginal upwarp with a sequence of post-rift Maastrichtian to Holocene sandstones, shales and minor carbonate rocks deposited in alternating regressions and transgressions (Kaki *et al.*, 2013). The offshore domain of the Benin basin contains Upper Cretaceous to Pleistocene post-rift sediments on top of Cenomanian to Santonian 'transitional' sediments, which are separated from the underlying Lower Cretaceous syn-rift and Paleozoic pre-rift sediments by the breakup unconformity (Kaki *et al.*, 2013).

Topography and geomorphology

The present-day Benin topography is characterised by predominantly low elevations (<500 m) and low relief (Fig. 1b, Fig. 2a). Moving north from sea-level at the southern coastline, the margin displays an upwarped topography gently rising over the 400 km seaward sloping limb of the marginal upwarp to an E-W trending crest with an elevation of c. 400─450 m, which acts as a continental drainage divide. The seaward slope of the divide is occupied by the Ouémé River catchment. North of the divide there is a modest decrease in elevation to c. 300 m towards the Niger River. The Dahomey Belt forms a topographic rise called the Atakora range in west Benin (Fig. 2a). The range arcs from N-S through eastern Togo to NE-SW in Benin. The boundary of the range is marked by a c. 300 m high, west facing escarpment.

Since the Late Cretaceous, several weathering phases have affected the West African landscape and produced lateritic duricrusts on the remnant topography (Beauvais & Chardon, 2013; Grimaud *et al.*, 2014, 2015). By dating these paleo-surfaces using Ar-Ar geochronology on their respective regoliths and measuring their dissection, denudational phases have been quantified since the Eocene and are characterised by very low overall rates of denudation (c. 2─20 m/Ma and mostly <10 m/Ma) (Beauvais & Chardon, 2013; Grimaud *et al.*, 2015, 2018). Flooding during Late Cretaceous marine transgressions (e.g., Ye *et al.*, 2017) suggests the topography was low-lying.

Methods

Apatite fission track and (U-Th-Sm)/He analysis

New AFT data (Table 1) were obtained from 18 samples along the Benin transect and multiple individual apatite grains from 12 of these samples were also dated using (U-Th-Sm)/He analysis (Table 2). Fission-track ages were obtained using the zeta-calibration external detector method (Hurford & Green, 1983). AFT ages were combined with length measurements of horizontal confined tracks (HCTs) to constrain thermal annealing of tracks through the AFT partial annealing zone (PAZ, 60─110±10 °C). The angle of HCTs to the crystallographic *c*-axis and D_{par} (length of the etch pit formed by tracks intersecting the polished grain surface) were also measured to correct for anisotropic annealing (Ketcham, 2005) and compositional influences on track annealing (Carlson *et al.*, 1999; Donelick *et al.*, 2005), respectively.

Apatite (U-Th-Sm)/He analysis was performed at the Scottish Universities Environmental Research Centre (SUERC) using laser heating and a quadropole mass spectrometer to extract and analyse He concentrations and isotopic dissolution ICP-MS was used to measure U, Th and Sm concentrations (e.g., Foeken *et al*., 2006). Durango standards were routinely analysed with a variation of 10%.

The range of temperatures between total diffusive loss and total retention of He in apatite define a partial retention zone (Wolf *et al.*, 1998). The upper and lower temperature limit of this zone is dependent on the size of the diffusion domain (i.e., grain size) (Reiners and Farley, 2001) and on the amount of cumulative radiation damage in the crystal (Shuster *et al.*, 2006; Flowers *et al.*, 2009; Gautheron *et al.*, 2009, 2013; Gerin *et al.*, 2017). Each apatite crystal therefore has a unique closure temperature, which can lead to significant single-grain AHe age dispersion depending on the thermal history (Fitzgerald *et al.*, 2006; Brown *et al.*, 2013).

QTQt Thermal History Model set-up

Thermal history models have been obtained for all samples analysed in this study using the Bayesian transdimensional MCMC approach of QTQt (Gallagher, 2012). Where available, AFT and single-grain AHe data for each sample were modelled together in a joint inversion. A multi-sample inversion was performed for three lower Paleozoic sandstone samples from an elevation profile (BN14, BN15 BN16) with the assumptions that the samples have resided at the same present-day temperature, have maintained their present-day vertical offset over time, and that the paleo-geothermal gradient was 25±10 °C. All other samples were modelled individually to allow for any lateral variations in the thermal history due to regional or local tectonic processes to be observed.

Our approach uses the multi-kinetic fission track annealing model of Ketcham *et al.* (2007), the radiation damage and annealing model for helium diffusion of Gautheron *et al.* (2009), and treats broken, 1-termination, crystals using a modified version of Beucher *et al.* (2013) described by Gallagher (2017). There remain several poorly understood factors that may affect the interpretation of the observed AHe age such as the influence of parent zonation, fluid inclusions, implantation from neighbouring grains, alpha-ejection, annealing of radiation damage defects, and their influence on diffusion at high concentrations. For this reason, we have allowed the observed apatite (U-Th-Sm)/He age to be resampled from a normal distribution centred on the measured age with 1σ equal to the estimated uncertainty on this age (Table 2). As a result of this treatment, the more robust AFT data will predominantly control the form of the thermal history with the He data having less influence. Full details of the thermal history model input are provided in the supporting material (SI-Table 1) following the recommendations of Flowers *et al.* (2015) and Gallagher (2016).

In the results section, we present the expected thermal history model for all samples, which is an average of all accepted models (see Gallagher, 2012, for details), alongside their data predictions (Figs. 3 to 6). For some samples, Cenozoic reheating events are observed in the expected model; however, they are often a consequence of averaging a subset of individual models that require reheating with other individual models that do not. To investigate the robustness of these heating events, we refer to the maximum posterior and/or the maximum likelihood models and assess whether the heating event is well constrained and consistent with nearby thermal histories and with the local geomorphology and geological constraints. The maximum posterior model shows the simplest model (fewest time-temperature (t-T) points) required to fit the data. The maximum likelihood model is the model that statistically best fits the data. The data predictions for posterior and maximum likelihood models and the summary graphics for the log-likelihood and number of t-T points for all models can be found in the Supplementary Information (SI-4, SI-5).

Constraints on the thermal history, based on geological and geomorphological observations, are included in the form of a t-T box (e.g., black boxes in Fig. 3 to 6) through which the thermal history paths must pass. Details on all constraints used are summarised in the Supplementary Information (SI-2, SI-Table 2). Sedimentary samples were constrained at surface temperatures (20±10 °C) at a time that reflects their stratigraphic age. Basement samples were given a broad initial t-T constraint of 900±100 Ma, 100±100 °C. The prevalence of basement lithologies across much of central Benin limits stratigraphic constraints being added to models. However, the location of some basement samples relative to the coastal basin and Iullemmeden Basin and careful consideration of geomorphic features provide important constraints for the models. For example, detailed investigation of lateritic paleo-landforms that formed and were subsequently dissected during the Cenozoic provide an independent estimate of the timing and magnitude of denudation after the mid-Eocene (c. 45 Ma; e.g., Beauvais & Chardon, 2013; Grimaud *et al.*, 2014, 2015, 2018) and can be used to constrain when samples were residing at surface temperatures. In many cases, the geomorphological constraints imply that no burial of the sample occurred during the early or late Cenozoic. Changing the time range of the prior input so that it extends only to the time that the rock reached the surface and remained there, rather than extending it to the present day, avoids artificially introducing structure in the thermal history over the time when the geomorphology requires thermal stability (or negligible thermal perturbation).

Denudation and burial estimates

A preferred thermal history path was chosen for all samples along the transect. This is typically the expected model, but the posterior model is selected when reheating events in the expected model are not well constrained or consistent with existing geological evidence (see Supplementary Information Table 1 for details). Using this t-T path and an estimate of the geothermal gradient, magnitudes of denudation or burial over different time intervals can be calculated (see SI-Table 3 for all denudation/burial data).

Estimating the geothermal gradient over space and time along eroded basement terrains is inherently uncertain (Łuszczak *et al.*, 2017). For simplicity, we use a value of 25 °C/km, which is consistent with global average geothermal gradients of 20–30 °C/km (Turcotte and Schubert, 2002) and with the estimated heat flow range in Benin (40–60 mW m^{-2}) (Lesquer *et al.*, 1990). We also assume the gradient is constant over the last 200 Ma in the absence of any evidence of volcanism and fluctuating geothermal gradients (Gunnell, 2003). Cooling rates were read directly from the preferred thermal history model. Estimates of the denudation/burial over a specific time interval were calculated using $\Delta Z = ((t_1 - t_2)/(T_1 - T_2)) * G$, where ΔZ = denudation (km), t_1 and t_2 are the expected temperatures (°C) at time T_1 and time T_2 (Ma), and G is the geothermal gradient (°C/km). These estimates of denudation/burial provide an approximation of the temporal and spatial patterns of erosion/deposition across the Benin margin. However, we acknowledge that uncertainties on these estimates can be anticipated from the uncertainty on paleo-temperature at a given time (defined by the 95% credible intervals), variations in upper crustal heat flow over space and time, and thermal properties of the eroded or deposited material (Łuszczak *et al.*, 2017).

Results

Apatite fission track and (U-Th-Sm)/He results

Apatite fission-track data are presented in Table 1, single grain age radial plots are provided in the Supplementary Information (SI-1), and track length distributions are displayed alongside the thermal history models (Fig. 3 to 6). Central AFT ages range from 106±5 to 401±45 Ma and mean track lengths (c-axis corrected) range from 12.4±0.7 and 14.4±0.1 μm. Several samples fail the chi-squared age homogeneity test (i.e., $P(\chi^2) < 0.05$); however, for many of these samples the single grain age dispersion is still relatively low (< 20%) and therefore the single grain ages are not considered to be overly dispersed. For samples that fail the chi-square test and have large single-grain age dispersion, this could be attributed to fission tracks in grains from sedimentary rocks, which have a different provenance, that have not been entirely annealed post-deposition (e.g., BN8 and BN14). For basement rocks, the variation in single grain ages may be linked to intra-sample compositional variations. The trend in AFT age with distance from the coast is characterised by Early to mid-Cretaceous (syn- to post-rift) ages along the southern 300 km coastal region (106 ± 5─132 ± 7 Ma) and older Devonian to Middle Jurassic (pre-rift) ages in the interior (168 ± 7─401 ± 45 Ma) (Fig. 2c). Further inland, an Early Cretaceous syn-rift AFT age is observed (BN6 = 130 ± 11 Ma).

Single-grain AHe ages, uncorrected for alpha-ejection, range from 22±3 (BN17-5) to 390±74 Ma (BN9-2) (see Table 2 for F_t corrected ages). The range of eU over the entire dataset is modest (2─40 ppm). Many single-grain AHe ages are younger or overlap within uncertainty with their equivalent AFT age. No individual factor (i.e., eU, grain size, fragmented crystal length) can be identified as the main control over the single-grain age dispersion and explain the individual AHe ages that are older than their AFT age (see Supplementary Information for plots of AHe age against eU and spherical equivalent radius (SI-3)). Overall, the AHe data broadly agree with the AFT data insomuch as Cretaceous aged AFT ages and Paleozoic AFT ages are complemented by similarly aged AHe data.

Thermal history models

Coastal basin

BN18 is a Maastrichtian sandstone from the coastal basin and therefore has experienced some burial after the sediments were delivered to the basin. Although the data from BN18 are limited we can say that (i) the AFT age is older than the stratigraphic age, (ii) the MTL is short (10.3±0.7 μm), and (iii) the four single-grain AHe ages can be split into two populations. As the AFT and AHe ages are older than the Maastrichtian age of deposition, the sample was not buried to an extent that would cause total track annealing or total He diffusion in apatite. Therefore, the two groups of the AHe ages could reflect a different provenance of the grains. As the data may have a strong provenance-related signal, the anomalously old AHe ages were modelled as a separate component from the AFT data and younger AHe ages and each component modelled simultaneously. This allows the 'older' apatite grains to have an independent pre-depositional history to the 'younger' grains but have a shared post-depositional history (Fig. 3). Two populations may also be present in the AFT data; however, given the low number of counted grains, multiple populations cannot be resolved. We have therefore assumed that the two grains from the younger AHe population are consistent with the whole sample AFT data (i.e., central age and MTL).

The expected model (Fig. 3) implies that following deposition in the Maastrichtian, the sample was heated to temperatures of c. 50 °C, before cooling until it resided at surface temperatures after 30 Ma. By splitting each component of the data (i.e., AFT data, young AHe grains and old AHe grains) we can sample independent pre-depositional thermal histories for each component of the data. The older population of AHe ages suggest extremely slow cooling rates, which extends back through the Paleozoic. The AFT and young AHe ages record a more rapid pre-depositional cooling history beginning at 150–160 Ma.

Seaward sloping limb of the marginal upwarp

BN1 was collected from basement rocks under the Maastrichtian shallow marine sediments of the coastal sedimentary basin and is therefore assigned a surface temperature constraint in the Late Cretaceous (72.5±2.5 Ma). The expected model shows that the onset of cooling was in the Middle Jurassic (c. 180–160 Ma). The model then shows steady monotonic cooling through the Cretaceous until it is forced to reach the surface during the Maastrichtian (Fig. 3). Given the credible intervals on the expected model below 60 °C, it is possible that the basement was exposed earlier in the mid- to

Late Cretaceous. After the Maastrichtian, the expected thermal history predicts that the sample was heated to temperatures of c. 50 °C by 30 Ma before cooling again to surface temperatures at 6 Ma. However, the geomorphic constraint that pins BN18 at the surface since 29 Ma is also likely to be applicable here and so any post-Maastrichtian reheating and cooling likely occurred between c. 70–30 Ma.

BN2 exhibits the same style of Cretaceous cooling as observed for BN1 and resided at low, near-surface temperatures (c. 40 °C) during Maastrichtian sedimentation (Fig. 3); however, no direct evidence is available to suggest that this sample was buried by these sediments and the posterior model does not require burial related heating at this time. Only very minor cooling to surface temperatures is shown from 45 to 6 Ma to reflect the c. 250 m of denudation implied by the local geomorphology.

BN3 and BN4 also show a thermal history dominated by Cretaceous cooling, which differs from BN1 and BN2 by having a more rapid cooling rate through the PAZ starting at c. 130–140 Ma (Fig. 3). Initially the samples cool rapidly to temperatures <60 °C over a period of 30 Myr before the rate of cooling slows through the mid to Late Cretaceous (c. 100–70 Ma).

BN17 and BN5 predict a similar time for the onset of cooling as BN3 and BN4 (i.e., Early Cretaceous). BN17 shows fairly rapid cooling between c. 130 and 110 Ma, bringing the sample from c. 110 to 60 °C. From the mid-Cretaceous to early Eocene (45 Ma) it is unclear from the expected model whether the sample experiences slight reheating or is held at temperatures of 60±5 °C. However, the posterior model suggests that slow, monotonic cooling could adequately reproduce the observed data. For BN5, the expected model shows that the initial cooling in the Early Cretaceous brings the sample to surface temperatures before it is heated to c. 45 °C at 20 Ma and then brought back to surface temperatures by 6 Ma. The maximum likelihood model also shows this thermal history; however, the posterior model shows that the sample need only be rapidly cooled to temperatures below the top of the PAZ (i.e., 60 °C) during the Early Cretaceous and then may experience slow monotonic cooling to present-day. A scenario with no reheating from the Late Cretaceous to the present is more consistent with surrounding samples (i.e., BN3 and BN4).

Interior

Beyond BN5, at approximately the crest of the marginal upwarp, there is a transition to older AFT ages (Fig. 2c) where samples retain thermal information from before the Early Cretaceous. The expected models for BN11 and BN12 are still relatively unconstrained during pre-Permian time, but at c. 300 Ma both samples were at elevated temperatures between c. 80 and 120 °C (Fig. 4). BN12 shows relatively rapid cooling through the PAZ over 250–200 Ma, followed by limited and slow cooling to the present day, whereas BN11 shows protracted cooling from c. 300 Ma to the present. Given the short distance between these samples (c. 30 km), the true rate of cooling from the Mesozoic to the present-day will likely be similar and lie somewhere between the two end-member scenarios shown by the individual models. We acknowledge the extremely poor data fit for two of the AHe ages for sample BN11 and find no common dispersion factor responsible for these anomalous ages. However, our treatment of the AHe data is such that even removing these anomalous grains does not change the expected model.

The onset of cooling for BN10 occurred in the Cambrian, significantly earlier than for BN11 and BN12. The expected model for BN10 shows that from c. 400 to 80 Ma, the sample was heated by around 10–15 °C; however, the model is poorly constrained through the Paleozoic and early Mesozoic. The maximum likelihood and maximum posterior models present two alternative scenarios. The maximum likelihood model shows the sample is cooled to the surface at 500 Ma, heated to 60 °C by 300 Ma, slowly cooled to 45 °C by 10 Ma before a final cooling episode to bring the sample to surface temperatures by the present day (Fig. 4). The maximum posterior model shows that after initially cooling to 50 °C by 350 Ma, the sample held at a constant temperature until 10 Ma when it is cooled to surface temperatures (Fig. 4). A consistent observation from these three models is that the sample passes through temperatures of c. 50 °C between 100 and 80 Ma; however, the exact thermal path the sample took to reach this temperature is poorly resolved by the thermochronology data because the cooling/heating occurs over very low temperatures not detected by the AFT and AHe systems.

Iullemmeden Basin margin

Samples BN6, BN7, BN8 and BN9 occur along the southern margin of the Iullemmeden Basin (Fig. 2b). BN6 and BN8 are Ordovician-Silurian sandstones and are, therefore inferred to have lain at the surface at this time. Given the planar, low sloping nature of the contact between the basin and underlying basement and the proximity of BN7 and BN9 to the sedimentary samples (<40 km), it is also deemed appropriate to constrain BN7 and BN9 as having been at the surface in Ordovician-Silurian time (490─420 Ma). The presence of Lower Cretaceous (c. 140─100 Ma) sediments on top of the basement <100 m from the sample location also implies that the BN6, BN7, BN8 and BN9 samples were at, or near, the surface in the Early Cretaceous.

During the Paleozoic, samples BN7, BN8 and BN9 experienced heating; however, the timing and magnitude differs for each sample (Fig. 5). The expected model for BN9 shows heating of around 60 °C from 485 to 435 Ma. The 95% credible intervals at this time cover the entire range of temperatures from surface temperatures to the base of the PAZ (i.e., c. 10─120 °C), suggesting that this heating event is not well constrained. The maximum posterior and maximum likelihood models for BN9 show two contrasting end-member scenarios. The maximum posterior shows no heating after the Ordovician, while the maximum likelihood shows burial to c. 135 °C from c. 435─430 Ma. From c. 375 Ma until the Early Cretaceous. The expected model shows slow, low magnitude cooling through the 45─25 °C window. Over this time, the range of possible temperatures defined by the 95% intervals is between 20 and 70 °C. This type of thermal history is also observed for sample BN7; however, the expected model for BN7 shows modest heating from c. 420─320 Ma before slow cooling to the surface until the Early Cretaceous. Both the maximum likelihood and posterior model for BN7 show that the sample was heated to c. 65 °C by c. 320─300 Ma.

The expected model for BN8 also captures heating of the basin from the Ordovician-Silurian to the end of the Carboniferous, suggesting that BN8 was heated to c. 100 °C by 300 Ma. The credible intervals for this model span the entire range of the PAZ, highlighting that the time and temperature of the burial event is poorly constrained. This can be ascribed to the low number of track lengths for this sample. Given the proximity of these three samples (60 km between BN9 and BN7), they should provide coherent information on the extent of Paleozoic burial. Considering the expected models and their credible intervals, we propose that the region spanning samples BN7, BN8 and BN9 was heated to maximum temperature of c. 65±5 °C from c. 455±35 to 300±20 Ma (Late Ordovician to latest Carboniferous).

The expected model (and posterior and maximum likelihood models) for BN6, which occurred further north in the Iullemmenden Basin, shows that over the Paleozoic the sample was heated to temperatures of c. 100‒120 °C, meaning that the sample was completely annealed prior to cooling at c. 160 Ma. Therefore, it is not clear when the sample reached temperatures higher than the base of the PAZ, or what was the maximum temperature that the sample reached prior to cooling. This would suggest a deeper cover of sediments in the Iullemenden Basin over BN6, which thins towards the south and where it covers BN7, BN8 and BN9.

During the early Mesozoic, prior to the deposition of Lower Cretaceous (120±20 Ma) sediments, BN7, BN8 and BN9 experience modest (c. 20‒40 °C) monotonic cooling. BN6 shows more rapid cooling of c. 80 °C starting at c. 160‒170 Ma. As the Cretaceous sediments are capped by bauxite (59‒45 Ma) to 'Intermediate' ferricrete (e.g., Beauvais and Chardon, 2013; 29‒24 Ma) (Fig. 1b) they are considered to have outcropped since c. 60 Ma and models are constrained at surface temperatures from this point to present-day. In the intervening period (i.e., 120±20 to 60 Ma) the expected models for BN6, BN7, BN8 and BN9 show reheating to maximum temperatures of c. 60 °C. However, the 95% credible intervals define a range spanning from surface temperatures to 60‒70 °C implying that there are acceptable models that require no reheating (i.e., burial) during the Cretaceous and others that do. While the extent and magnitude of burial related heating in the mid- to Late Cretaceous (c. 120‒70 Ma) is not fully resolved, the available data suggests that if the samples were reheated during this time they reached a maximum temperature of at most 60‒70 °C.

Atakora Range

BN14, BN15 and BN16 share the same late Proterozoic – early Cambrian stratigraphic age, form an elevation profile covering 300 m and are jointly inverted (Fig. 6). From surface temperatures at c. 550 Ma, the samples were heated to approximately 80‒90 °C by 340‒300 Ma and then cooled steadily to surface temperatures by 45 Ma. The timing and magnitude of burial is similar to that seen during the Paleozoic in the interior samples (e.g., BN11) and along the Iullemmenden Basin (e.g., BN8). The expected model for BN13 records a phase of more rapid cooling beginning at c. 220 Ma, which is similar to rapid cooling in the Late Triassic observed for BN12 (Fig. 4). While the expected models for BN13 and BN12 show almost no cooling through the post-Triassic to Mesozoic period (i.e., 180–70 Ma), BN13 shows a much more pronounced second phase of cooling from 70 Ma to the present day. The posterior model for BN13 does not require this two-stage history and suggests that a simple model of monotonic cooling, more consistent with that observed for the Atakora profile, is also possible. Although some aspects of the Jurassic to present-day thermal history for these samples, and BN12 and BN11, are unresolved it can be said that samples in this region remained at colder temperatures than c. 60 °C. They did not record the larger magnitude and faster rate of Early Cretaceous cooling observed in coastal samples or reheating linked to burial of the Iullemmeden Basin in the mid- to Late Cretaceous (see above).

Denudation and burial estimates

Denudation and burial estimates from thermal histories constrained by thermochronology and geomorphological data are shown on a coast-perpendicular profile across Benin (Fig. 7) and show cumulative thicknesses over different time intervals since 200 Ma. Time-slices were chosen to broadly complement the time intervals chosen for the Paleogeographical reconstruction of Ye *et al.* (2017). However, due to the temporal uncertainty and resolution of the models we do not feel it is prudent to produce a denudation estimate for each and every time interval presented by Ye *et al.* (2017), particularly those lasting just a few Myr. For many samples along the seaward sloping limb , which have experienced significant cooling in the Early Cretaceous (i.e., samples that were exhumed from below the base of the PAZ at this time), pre-Early Cretaceous (>140 Ma) denudation-related cooling has not been recorded. In such cases, an estimated denudation magnitude for the 200–140 Ma time interval is made by interpolation using adjacent samples that have recorded cooling at this time. Estimates from sample BN1 and BN2 predict that a thickness of around 1.5 km was removed over the 200–140 Ma interval.

A striking pattern of total denudation across the margin is evident, with the largest total magnitudes (up to 5 km) being observed along the coastal basin and the seaward sloping limb and lower magnitudes (<1.5 km) observed further inland (Fig. 7). Between 0 and c. 350 km inland of the coast (Fig. 7), most of this denudation took place during the Cretaceous (145–65 Ma), with rates as high as

c. 86 m/Myr (BN3) observed during the Early-Cretaceous (140─100 Ma) pre- and syn-rift phase. During the Early Cretaceous, average denudation rates of 44 m/Myr are predicted along the seaward sloping limb, while inland at the crest of the marginal upwarp (i.e., BN10, BN11 and BN12) they are considerably less (0─11 m/Myr). Over the entire Mesozoic, average denudation rates for the marginal upwarp crest samples and the samples from the Atakora Range (i.e., BN13, BN14, BN15, BN16) are < 12 m/Myr and are consistent with low rates of denudation-driven cooling constrained by AFT data from the cratonic interior and lateritic landscape of Burkina Faso (Fig. 1, Gunnell, 2003).

High denudation rates, similar to those observed along the coastal margin are observed at the margin of the Iullemmeden Basin in sample BN6 over 140-120 Ma (c. 74 m/Myr). The amount of reheating experienced by BN6 and the other samples along the margin of the Iullemmenden Basin (i.e., BN7, BN8 and BN9) during the mid-Late Cretaceous (120─70 Ma) is not well constrained (0 to 60 °C of heating). However, this region of northern Benin may have been flooded by the 'Trans Saharan Seaway' during the Late Cretaceous (Ye *et al.*, 2017) and shallow marine sediments may have buried samples BN6, BN7, BN8 and BN9. Using the expected thermal history model, a conservative estimate for the amount of burial is determined to be c. 1─1.2 km. The temperature range defined by the 95% credible intervals means that the estimated amount of burial ranges from 0 to 2 km and that this would likely vary laterally across the sample population.

Similarly, BN18, taken from the Late Cretaceous sediments in the coastal basin, and BN1, on the fringes of this basin, were almost certainly buried in the Late Cretaceous to earliest Cenozoic; however, the amplitude of the burial is not well constrained by the models. Based on the expected model for these samples, during the Cenozoic they were buried under 1─1.2 km of sediment, which was then removed. Cenozoic denudation rates are variable across Benin but are ≤20 m/Myr, consistent with previous estimates from Benin and from Burkina Faso (Gunnell, 2003; Beauvais & Chardon, 2013; Grimaud *et al.*, 2018).

Discussion

Our thermal histories provide insights into Mesozoic and Cenozoic denudation and burial that can be discussed within the framework of the Benin's pre-, syn- and post-rift tectonic evolution. The Paleozoic history is more difficult to resolve because many samples (e.g., along the 'seaward sloping limb' (Fig. 3), BN11 and BN12 from the 'interior' (Fig. 4), BN6 (Fig. 5) at the margin of the Iullemmeden Basin, and BN13 from the 'Atakora Range' (Fig. 6)) were heated to such an extent that their Paleozoic thermal histories were erased.

Paleozoic sediments are observed in the Volta and Iullemmeden basins, further north in Mali, southern Algeria and Niger, and along the Guinea continental margin (Fig. 1a). Although the amount of heating of samples BN7, BN8 and BN9 is not fully resolved, the models show that they were heated during the Paleozoic, albeit not to a sufficient depth to reset the apatite thermochronometers. A Paleozoic sedimentary cover could have feasibly covered the entire Benin marginal upwarp with a thickness that was greater across southern Benin and in northernmost Benin and Niger. Burial during the Paleozoic can be linked to the development and infilling of basins during and following the Pan-African orogeny (Deynoux *et al.*, 2006). Later regional deformation across West Africa related to the Variscan Orogeny at c. 300 Ma and focused along the West African Craton boundary (Ennih & Liégeois, 2008) may also have led to greater burial of the basement during the late Paleozoic.

In the early Mesozoic, the early stages of rifting and continental breakup were initiated in the Central Atlantic (Labails *et al.*, 2010), and were associated with the emplacement of magmatic rocks (lava flows, sill provinces and dikes) across the Guinea-Liberia margin (Jourdan *et al.*, 2009). In southern Benin, the CAMP is limited to some NNE–SSW-trending dikes (Knight *et al.*, 2004; Jourdan *et al.*, 2009); however, because of possible erosion the volume and distribution of magma during this event may be underestimated (Leleu *et al.*, 2016). East of the estimated extent of the CAMP (Fig. 1a), are 213–141 Ma-aged granites on the Nigerian Shield (Rahaman *et al.*, 1984) and 215–166 Ma-aged granites on the Hoggar Shield (Liégeois *et al.*, 1991; Ye *et al.*, 2017). The regional extent and duration over which igneous material was emplaced suggests that significant upwelling in the asthenosphere was present during the Middle Triassic to Early Cretaceous, synchronous with major rift tectonics, and could have driven uplift and concomitant denudation in Benin at this time. The only samples recording cooling as early as the Middle Triassic to Jurassic are found on the crest of today's marginal upwarp (e.g., BN12, BN13; onset of cooling 230–200 Ma) and along the seaward sloping limb (e.g., BN1, BN2; onset of cooling: 180–170 Ma). Other samples may have experienced cooling at this time but were too hot (> 100 °C, e.g., BN3) or too cold (< 60 °C, e.g., BN7) to constrain this cooling.

In the early stages of rifting through to the main rift phase, vertical motions may be related to mantle processes such as convection during crustal thinning or thermal relaxation and may have been spatially complex and episodic (e.g., Todd & Keen 1989; Basile *et al.*, 1993; Gadd & Scrutton, 1997). Also, tectonic uplift is possible as pure strike-slip movement along transform faults is rare and will likely involve either a component of isostatic uplift after tectonic unloading or a transition to a transpressional regime during its evolution. Both have been reported to have occurred along the Romanche transform fault (e.g., Mascle *et al.*, 1987; Clift & Lorenzo, 1999; Antobreh *et al.*, 2009; Nemčok *et al.*, 2013). Vertical movements along the transform fault may have produced a steep, c. 1-km-high escarpment, creating short-wavelength relief over tens of kilometres, which experienced rapid erosion (e.g., Basile & Allemand, 2002; Peulvast *et al.*, 2009; Ye *et al.*, 2017).

The early stages of rifting (140─120 Ma) and main rift phase (120─100 Ma) along the Equatorial Atlantic, which involved movement along ENE-trending transform faults and NW- to W-trending normal faults (relative to Africa's present-day position) (Ye *et al.*, 2017), coincide with the timing of greatest denudation along the seaward slope of the present-day marginal upwarp. The spatial pattern of AFT data and estimates of denudation from the coast to the present-day upwarp crest (Fig. 2c, Fig. 7) are consistent with enhanced erosion seaward of an interior continental drainage divide during the pre to syn-rift phase (c. 140─100 Ma) (Gilchrist & Summerfield, 1990; Gallagher & Brown, 1999; van der Beek *et al.*, 2002; Ye *et al.*, 2017). Although the location of a Paleo-drainage divide is speculative, the location could be approximated as being where Early Cretaceous denudation rates rapidly decrease between BN5 and BN12/BN11, which is close to the location of the present-day crest of the marginal upwarp (Fig. 7). Chardon *et al.* (2016) argue that a continental divide coinciding with the crest of the present-day marginal upwarp was established in the mid-Eocene. Our data suggests that the geometry of the marginal upwarp may have been created earlier, during the pre- to syn-rift phase and preserved due to a flexural isostatic response to asymmetric erosion on either side of the crest (e.g., Braun, 2018). Flexural isostasy in response to erosional unloading of the margin and deposition in offshore basins can also be responsible for maintaining high magnitudes of denudation throughout the Cretaceous across the seaward sloping limb (van Balen *et al.*, 1995; van der Beek *et al.*, 1995; Braun *et al.*, 2013).

Ye *et al.* (2017) produced Paleogeographical reconstructions of the West-African margins and showed the persistence of long-wavelength marginal upwarps that were formed at the time of rifting and were sustained or possibly reactivated during the post-rift phase. The largest upwarp wavelengths, between 1000 to 1400 km, are observed along the Guinea-Liberia and Ivory Coast Equatorial margin segments, whereas shorter wavelengths are observed north along the Senegalese and Congo segments related to the Central and South Atlantic margins, respectively. The long wavelengths observed across the Leo-Man shield (Fig. 1a) may extend across the Benin transect; however, variations in the upwarp wavelength and geometry may occur due to greater amounts of thermal relaxation and lithospheric strengthening along the older Ghana-Benin margin segment of the Equatorial Atlantic margin, the transform-controlled style of rifting along this margin and interaction with the Congo upwarp segment along the South Atlantic margin (Ye *et al.*, 2017). The flexural response advocated here is more consistent with the effects of the rift-related long-wavelength upwarp across the Leo-Man shield extending across the Benin sector of the margin. Neogene uplift of the Congo South Atlantic upwarp does not appear to have had an influence on the erosion history across Benin. The presence of Early Cretaceous (150─135 Ma) kimberlites across the Leo-Man shield link asthenospheric processes to thermo-chemical dynamics in the lithospheric mantle. Buoyancy in the lithospheric mantle may have provided secondary support to the upwarp (e.g., Ault *et al.*, 2015; Ye *et al.*, 2017); however, limited intrusive material preserved in Benin at this time casts doubt on the regional extent of active mantle processes at this time.

The interaction of short wavelength deformation processes acting over different timescales such as narrow rift flanks (c. 10─100 km) produced by flexure during lithospheric stretching forming escarpments (e.g., Rouby *et al.*, 2013), in addition to the influence of climate and lithology on surface processes, will have resulted in more complex spatial and temporal patterns of erosion than described here (e.g., Abrahami *et al.*, 2016). Due to the coverage and resolution of our data we can only resolved the longer wavelength processes dominating the long-term signal of erosion and deposition (e.g., Ye *et al.*, 2017).

The material eroded during the Early to mid-Cretaceous (c. 140─100 Ma) would have fed clastic sediments into the offshore Benin Basin (e.g., Kaki *et al.*, 2013) and filled the syn-rift NW to N trending grabens formed during transcurrent and extensional faulting (Davison, 2005; Kaki *et al.*, 2013; MacGregor *et al.*, 2003; Brownfield & Charpentier, 2006; Ye *et al.*, 2017). A regional unconformity at the spanning the Aptian-Albian boundary to Cenomanian (c. 113─93 Ma) sequences is ubiquitous across the offshore Equatorial Atlantic margins and marks the time of breakup (Mascle *et al.*, 1987; Nemčok *et al.*, 2013; Moulin *et al.*, 2010) and separates deformed and faulted basement and Lower Cretaceous syn-rift sediments from younger ‘transitional’ and drift sequences (Kaki *et al.*, 2013). The main deformation phase of rifting in the Early Cretaceous, ended abruptly at the time of breakup and lead to the formation of the breakup unconformity (Mascle *et al.*, 1987).

Based on our thermal history paths, denudation rates along the seaward sloping limb of the margin are inferred to have been around 26 m/Myr during the 100–85 Ma interval, which is a decrease from the Early Cretaceous (140–100 Ma, 44 m/Myr). Apatite fission-track data from two boreholes through the marginal ridge in the offshore Ivory Coast-Ghana segment suggest rapid erosion-driven cooling at the beginning of the main rift phase (c. 120–115 Ma, Clift *et al.*, 1998). Tracks in samples from the offshore seaward-sloping shoulder of the marginal ridge are entirely annealed due to burial under Aptian-Albian sediments (125–100 Ma) (Bigot-Cormier *et al.*, 2005). Rapid retrogressive erosion of a prominent oceanic basement ridge along the southern margin of the Deep Ivorian Basin between 85 and 65 Ma, driven by flexural uplift of the shoulder, was advocated by Bigot-Cormier *et al.* (2005) to explain a later cooling recorded by their fission-track data. Our estimates of the timing and rates of denudation, combined with insights from offshore AFT data, suggest that the most significant denudation onshore coincided with the major rift-related deformation phase. This was followed by slower rates of denudation after breakup when the margin underwent post-rift subsidence.

Beyond Benin’s interior region of low denudation, the thermal history of BN6, at the margin of the Iullemmeden Basin, suggests that around 2 km of denudation occurred during the Early Cretaceous (predominantly during the Valanginian to Barremian, 140–120 Ma). This denudation may be linked to the erosion of elevated shoulders along the Gao rift (Fig. 1a), which was active at this time (Guiraud and Maurin, 1992; Heine *et al.*, 2013; Ye *et al.*, 2017). Samples at the margin of the Iullemmeden Basin were then potentially buried by non-marine sediments of the Saharan Basin (Ye *et al.*, 2017) during middle Aptian to Albian (120–100 Ma) subsidence triggered by changes in the intra-plate stress-field and tensional forces linked to Atlantic rifting (Moody and Sutcliffe, 1991; Guiraud *et al.*, 2005). Minor offsets on the Kandi Fault may also have occurred at this time, creating a small fault-bounded basin (Konate *et al.*, 2003). Transgressions coming from the north during the late Cenomanian to early Santonian (100–85 Ma) led to further burial beneath marine sediments (Guiraud *et al.*, 2005; Frizon de Lamotte *et al.*, 2015; Ye *et al.*, 2017).

From the end of the Cretaceous, erosion rates across the margin and interior are low and it is likely that by this time the present-day low-relief and low elevation first order topography had been formed. During the Late Cretaceous and Cenozoic, transgressions and regressions (Davison, 2005; Bumby & Guiraud, 2005) resulted in episodes of deposition and erosion of coastal basin sediments. Samples BN18 and BN1 record modest heating and cooling over this time and suggest that the total thickness of sediments in the coastal basin that covered the now exposed basement was c. 1 km. It also suggests that the northern extent of the basin margin being, at most, situated 100─150 km inland from the present-day coastline.

Greenhouse climate conditions during the late Paleocene to early Eocene and a cooler but still tropical climate in the late Oligocene and Miocene, coupled with relative stability of the margin, caused the development of sequential laterite weathering surfaces on the relict Cretaceous topography (Beauvais & Chardon, 2013; Chardon *et al.*, 2016). Erosion in the intervals between these weathering phases was relatively minor (c. 2─10 m/Myr), with localised river incision dissecting the surfaces (Beauvais & Chardon, 2013; Grimaud *et al.*, 2014, 2015, 2018). Offshore, several post-Cretaceous unconformities are the result of alternating regressions and transgressions (Kaki *et al.*, 2013). A major offshore erosional unconformity between the late Eocene-early Oligocene and the Miocene, indicates a depositional hiatus coeval with the proposed timing of post-Oligocene uplift linked to intraplate hot spots (e.g., Burke & Gunnell, 2008). The presence and regional extent of mantle plumes capable of driving uplift in West Africa have been debated (Zhao, 2007; Forte *et al.*, 2010).

Alternative models for the development of the West African basin and swell topography have been based on the propagation of intraplate stress during the Eocene Africa-Europe collision, potentially coupled with edge-driven convection (Liegois *et al.*, 2005, Rougier *et al.*, 2013). The onshore denudation record inferred from thermochronology and geomorphology and offshore sedimentation record suggests that, regardless of the mechanism, any surface uplift during the late Eocene-Oligocene did not trigger erosion on the scale of several kilometres. A slight increase in the cooling rates for some inland samples could be linked to an increase in post-Eocene erosion. An offshore erosional surface at the top of early Oligocene sediments, which extends into the Neogene, suggests that erosion related to marine regressions occurred continuously or in phases through the late Cenozoic (Fig. 1b). Inland, rates of erosion > 20 m/Myr are primarily found on the actively uplifting Hoggar swell (Chardon *et al.*, 2016; Grimaud *et al.*, 2018).

Conclusions

We have presented new apatite thermochronology data from samples across the entire Benin marginal upwarp and combined the insights they have provided on rock cooling with geomorphological constraints on Cenozoic erosion to estimate the timing and magnitude of denudation over the last 200 Myr. The main episode of denudation occurred during rifting and continental breakup in the Early Cretaceous. From 140─100 Ma, a thickness of up to 4 km was removed from the seaward sloping limb of the marginal upwarp as a result of the rapid erosion of the marginal upwarp. At approximately the same position of the present-day upwarp crest, Early Cretaceous denudation is an order of magnitude lower than at the coastal margin, suggesting that the drainage divide could be long-lived and could have influenced the style of landscape evolution along the continental margin. The thermal histories obtained from the models allow modest burial of basement rocks under a coastal basin during the Late Cretaceous to early Cenozoic (85─45 Ma) and under the inland Iullemmeden Basin during the mid-Cretaceous (120─85 Ma), but they limit the thickness of sediment to c. 1─1.5 km, which was subsequently removed. We suggest that by the Eocene the present-day first-order topography of the Benin sector of the West-African transform margin had developed. Relative tectonic stability and changing climatic conditions led to the formation of lateritic surfaces on the remnant topography.These were sequentially dissected to form the present-day relief. Surface uplift of the margin and continental interior (e.g., Hoggar swell) related to underlying mantle plumes or lithospheric buckling may have occurred, but we suggest regional erosion rates since the Eocene were ≤ 20 m/Myr, consistent with previous estimates.

Acknowledgements

This study was funded by Total Exploration and Production through the Transform Source-to-Sink Project (TS2P). We thank the Office Béninois des Recherches Géologiques et Minières (OBRGM) and the Direction Générale des Mines (DGM) as well as the members of the Geology department of the Université Abomey Calavi for support and advice during the 2014 field trip. I. Gnammi is thanked for his participation in the fieldwork. We thank Fin Stuart and Luigia Di Nicola at the Scottish Universities Environmental Research Centre for their assistance during (U-Th-Sm)/He analysis. Rémi Leprêtre and Jean-Paul Liégeois are thanked for providing detailed and constructive reviews of this paper.

Fig. 1: (**a**) Regional geological and tectonic map of West Africa (after Ye *et al.*, 2017). (**b**) Geological cross-section across the Benin margin showing topo-bathymetry, post-Proterozoic geology, and sample locations. The offshore part to the section is based on unpublished seismic data (Huyghe, 2016, Internal Report). Interpolation of the two regional lateritic land surfaces is shown. In red is the "African surface", which underwent bauxitic weathering until c. 45 Ma, and in blue is the "Intermediate Surface", which underwent weathering until c. 24 Ma (Chardon *et al.*, 2016).

Fig. 2: (**a**) Topographic and (**b**) geological map of Benin and neighbouring areas, sample locations and data (adapted from Choubert & Faure-Muret, 1988 and Thieblemont *et al.*, 2016). KF: Kandi Fault. B: Benin, BF: Burkina Faso, G: Ghana, Na: Nigeria, Ni: Niger, T: Togo. CB: Coastal Basin, Iullemmeden Basin, KB: Kandi Basin. (**c**) Transect X-Y showing the projection of samples onto topographic profiles and AFT age, MTL and AHe age range across the section.

Fig. 3: Results of thermal history modelling for from the seaward sloping limb of the marginal upwarp. Left-hand plots: Thermal history models region. Blue line is the expected model; magenta lines are 95% credible intervals on the expected model. For BN18, the blue curve (with cyan 95% credible intervals) and red curve (with magenta 95% credible intervals) are the expected models for the younger and older populations of AHe ages. Red box represents the prior information on temperature and time. Black boxes are additional geological constraints. Yellow line is the maximum posterior model and grey line is the maximum likelihood model. Central plots: Histograms are the observed track-length distributions; red and grey curve indicates the predicted track-length distributions and 95% credible intervals. Right-hand figures: Observed vs. predicted age data; circles represent AFT ages, squares are single-grain AHe ages. Horizontal black lines are the 1σ uncertainty on the observations; vertical black lines are the range of predicted values for all models. Coloured bars are the range of resampled observed ages. Grey line is the one-to-one correlation line.

Fig. 4: Thermal history models for samples interior samples. See Fig. 3 for symbology details.

Fig. 5: Thermal history models for samples from the margin of Iullemmeden Basin. See Fig. 3 for symbology details.

Fig. 6: Thermal history models for samples from the margin of the Volta Basin. See Fig. 3 for symbology details.

Fig. 7: Estimates of cumulative denudation along X-Y transect (c.f. Fig. 2c) over specified time intervals assuming a geothermal gradient of 25 °C/km. Lower image shows the topography along the section and sample location projected onto the line of section.

Table 1: *Apatite fission-track data*.

Table 2: *Apatite (U-Th-Sm)/He data*.

References

Abrahami, R., van der Beek, P., Huyghe, P., Hardwick, E. & Carcaillet, J. 2016. Decoupling of long-term exhumation and short-term erosion rates in the Sikkim Himalaya. *Earth and Planetary Science Letters*, **433**, 76–88, doi: 10.1016/j.epsl.2015.10.039.

Alidou, S., Lang, J., Bonvalot, J., Roman, E. & Seilacher, A. 1991. Marine influences in the so-called continental sediments of the Paleozoic-Mesozoic Kandi Basin (Northern Benin-West Africa). *Journal of African Earth Sciences (and the Middle East)*, **12(1–2)**, 55–65, doi: 10.1016/0899-5362(91)90057-6

Antobreh, A.A., Faleide, J.I., Tsikalas, F. & Planke, S. 2009. Rift–shear architecture and tectonic development of the Ghana margin deduced from multichannel seismic reflection and potential field data. *Marine and Petroleum Geology*, **26(3)**, 345–368, 10.1016/j.marpetgeo.2008.04.005.

Attoh, K., Samson, S., Agbossoumondé, Y., Nude, P.M. & Morgan, J. 2013. Geochemical characteristics and U–Pb zircon LA-ICPMS ages of granitoids from the Pan-African Dahomeyide orogen. *West Africa. Journal of African Earth Sciences*, **79**, 1–9, doi: 10.1016/j.jafrearsci.2012.09.015.

Ault, A.K., Flowers, R.M. & Bowring, S. A. 2015. Synchroneity of cratonic burial phases and gaps in the kimberlite record: Episodic magmatism or preservational bias?. *Earth and Planetary Science Letters*, **410**, 97–104, doi: 10.1016/j.epsl.2014.11.017.

Barros, L.V., Assumpção, M. *et al*. 2015. The Mara Rosa 2010 GT-5 earthquake and its possible relationship with the continental-scale Transbrasiliano lineament. *Journal of South American Earth Sciences*, **60**, 1–9, doi: 10.1016/j.jsames.2015.02.002.

Basile, C. & Allemand, P. 2002. Erosion and flexural uplift along transform faults. *Geophysical Journal International*, **151(2)**, 646–653, doi: 10.1046/j.1365-246X.2002.01805.x.

Basile, C., Mascle, J. & Guiraud, R. 2005. Phanerozoic geological evolution of the Equatorial Atlantic domain. *Journal of African Earth Sciences*, **43(1–3)**, 275–282, doi: 10.1016/j.jafrearsci.2005.07.011.

Basile, C., Mascle, J., Popoff, M., Bouillin, J.P. & Mascle, G. 1993. The Ivory Coast-Ghana transform margin: a marginal ridge structure deduced from seismic data. *Tectonophysics*, **222(1)**, 1–19, doi: 10.1016/0040-1951(93)90186-N.

Beauvais, A. & Chardon, D. 2013. Modes, tempo, and spatial variability of Cenozoic cratonic denudation: The West African example. *Geochemistry, Geophysics, Geosystems*, **14(5)**, 1590–1608, doi: 10.1002/ggge.20093.

Beauvais, A., Ruffet, G., Hénocque, O. & Colin, F. 2008. Chemical and physical erosion rhythms of the West African Cenozoic morphogenesis: The ^{39}Ar-^{40}Ar dating of supergene K-Mn oxides. *Journal of Geophysical Research: Earth Surface*, **113(F4)**, doi: 10.1029/2008JF000996

Beucher, R., Brown, R.W., Roper, S., Stuart, F. & Persano, C. 2013. Natural age dispersion arising from the analysis of broken crystals: Part II. Practical application to apatite (U–Th)/He thermochronometry. *Geochimica et Cosmochimica Acta*, **120**, 395–416, doi: 10.1016/j.gca.2013.05.042.

Bigot-Cormier, F., Basile, C., Poupeau, G., Bouillin, J.P. & Labrin, E. 2005. Denudation of the Côte d'Ivoire–Ghana transform continental margin from apatite fission tracks: *Terra Nova*, **17**, 189–195, doi:10.1111/j.1365-3121.2005.00605.x.

Bonatti, E. 1996. Anomalous opening of the Equatorial Atlantic due to an equatorial mantle thermal minimum. *Earth and planetary science letters*, **143(1-4)**, 147–160, doi: 10.1016/0012-821X(96)00125-2.

Braun, J. 2018. A review of numerical modeling studies of passive margin escarpments leading to a new analytical expression for the rate of escarpment migration velocity. *Gondwana Research*, **53**, 209–224, doi: 10.1016/j.gr.2017.04.012.

Braun, J., Deschamps, F., Rouby, D. & Dauteuil, O. 2013. Flexure of the lithosphere and the geodynamical evolution of non-cylindrical rifted passive margins: Results from a numerical model incorporating variable elastic thickness, surface processes and 3D thermal subsidence. *Tectonophysics*, **604**, 72–82, doi: 10.1016/j.tecto.2012.09.033.

de Brito Neves, B.B. & Fuck, R.A. 2014. The basement of the South American platform: Half Laurentian (N-NW)+ half Gondwanan (E-SE) domains. *Precambrian Research*, **244**, 75–86, doi: 10.1016/j.precamres.2013.09.020.

Brown, R.W., Beucher, R., Roper, S., Persano, C., Stuart, F. & Fitzgerald, P. 2013. Natural age dispersion arising from the analysis of broken crystals. Part I: Theoretical basis and implications for the apatite (U–Th)/He thermochronometer. *Geochimica et Cosmochimica Acta*, **122**, 478–497, doi: 10.1016/j.gca.2013.05.041.

Brownfield, M.E. & Charpentier, R.R., 2006, Geology and total petroleum systems of the West-Central Coastal Province (7203), West Africa. *U.S. Geological Survey Bulletin 2207-B*, 52 p.

Bumby, A.J. & Guiraud, R. 2005. The geodynamic setting of the Phanerozoic basins of Africa. *Journal of African Earth Sciences*, **43(1)**, 1–12, doi: 10.1016/j.jafrearsci.2005.07.016.

Burke, K. & Gunnell, Y. 2008. *The African erosion surface: a continental-scale synthesis of geomorphology, tectonics, and environmental change over the past 180 million years. Geological Society of America Memoirs*, **201**, 1–66 doi: doi.org/10.1130/2008.1201.

Caby, R. 1989. Precambrian terranes of Benin-Nigeria and northeast Brazil and the Late Proterozoic south Atlantic fit. *In*: Dallmeyer, R.D. (ed) *Terranes in the Circum-Atlantic Paleozoic Orogens. Geological Society of America Special Papers*, **230**, 145–158, doi: 10.1130/SPE230-p145.

Carlson, W.D., Donelick, R.A. & Ketcham, R.A. 1999. Variability of apatite fission-track annealing kinetics: I. Experimental results. *American mineralogist*, **84(9)**, 1213–1223, doi: 10.2138/am-1999-0901.

Ceraldi, T.S., Hodgkinson, R. & Backé, G. 2017. The petroleum geology of the West Africa margin: an introduction. *In:* Ceraldi, T.S., Hodgkinson, R. & Backé, G. (eds) *The petroleum geology of the West Africa margin.* Geological Society, London, Special Publications, **438(1)**, 1-6, doi: 10.1144/SP438.11.

Chardon, D., Grimaud, J.L., Rouby, D., Beauvais, A. & Christophoul, F. 2016. Stabilization of large drainage basins over geological time scales: Cenozoic West Africa, hot spot swell growth, and the Niger River. *Geochemistry, Geophysics, Geosystems*, **17(3)**, 1164–1181, doi: 10.1002/2015GC006169.

Choubert, G. & Faure-Muret, A. 1988. International Geological Map of Africa (third edition): Commission for the Geological Map of the World (CCGM)/UNESCO, scale 1:5,000,000.

Clift, P.D. & Lorenzo, J.M. 1999. Flexural unloading and uplift along the Côte d'Ivoire-Ghana Transform Margin, equatorial Atlantic. *Journal of Geophysical Research: Solid Earth*, **104(B11)**, 25257–25274, doi: 10.1029/1999JB900247.

Clift, P.D., Carter, A. & Hurford, A.J. 1998. Apatite fission track analysis of Sites 959 and 960 on the Transform continental margin of Ghana, West Africa. In: Mascle, J., Lohmann, G.P. and Moullade, M. (eds), *Proceedings of the Ocean Drilling Program, Scientific Results*, **159**, doi: 10.2973/odp.proc.sr.159.004.1998.

Cordani, U.G., Pimentel, M.M., de Araújo, C.E.G. & Fuck, R.A. 2013. The significance of the Transbrasiliano-Kandi tectonic corridor for the amalgamation of West Gondwana. *Brazilian Journal of Geology*, **43(3)**, 583–597, doi: 10.5327/Z2317-48892013000300012.

Davison, I. 2005. Central Atlantic margin basins of North West Africa: geology and hydrocarbon potential (Morocco to Guinea). *Journal of African Earth Sciences*, **43(1)**, 254–274, doi: 10.1016/j.jafrearsci.2005.07.018.

Deynoux, M., Affaton, P., Trompette, R. & Villeneuve, M. 2006. Pan-African tectonic evolution and glacial events registered in Neoproterozoic to Cambrian cratonic and foreland basins of West Africa. *Journal of African Earth Sciences*, **46(5)**, 397–426, doi: 10.1016/j.jafrearsci.2006.08.005.

Donelick, R.A., O’Sullivan, P.B. & Ketcham, R.A. 2005. Apatite fission-track analysis. *Reviews in Mineralogy and Geochemistry*, **58(1)**, 49-94, doi: 10.2138/rmg.2005.58.3.

Edwards, R.A., Whitmarsh, R.B. & Scrutton, R.A. 1997. The crustal structure across the transform continental margin off Ghana, eastern equatorial Atlantic. *Journal of Geophysical Research: Solid Earth*, **102(B1)**, 747–772, doi: 10.1029/96JB02098.

Ennih, N. & Liégeois, J.P. 2008. The boundaries of the West African craton, with special reference to the basement of the Moroccan metacratonic Anti-Atlas belt. *In*: Ennih, N. & Liégeois, J.P. (eds) *The Boundaries of the West African Craton*. Geological Society, London, Special Publications. **297(1)**, 1-17, doi: 10.1144/SP297.1.

Fairhead, J.D., Green, C.M., Masterton, S.M. & Guiraud, R. 2013. The role that plate tectonics, inferred stress changes and stratigraphic unconformities have on the evolution of the West and Central African Rift System and the Atlantic continental margins. *Tectonophysics*, **594**, 118–127, doi: 10.1016/j.tecto.2013.03.021.

Farley, K.A., Wolf, R.A. & Silver, L.T. 1996. The effects of long alpha-stopping distances on (U-Th)/He ages. *Geochimica et Cosmochimica Acta*, **60(21)**, 4223–4229, doi: 10.1016/S0016-7037(96)00193-7.

Fitzgerald, P.G., Baldwin, S.L., Webb, L.E. & O'Sullivan, P.B. 2006. Interpretation of (U–Th)/He single grain ages from slowly cooled crustal terranes: a case study from the Transantarctic Mountains of southern Victoria Land. *Chemical Geology*, **225(1)**, 91–120, doi: 10.1016/j.chemgeo.2005.09.001.

Flowers, R.M., Farley, K.A. & Ketcham, R.A. 2015. A reporting protocol for thermochronologic modeling illustrated with data from the Grand Canyon. Earth and Planetary Science Letters, **432**, 425‒435, doi: 10.1016/j.epsl.2015.09.053.

Flowers, R.M., Ketcham, R.A., Shuster, D.L. & Farley, K.A. 2009. Apatite (U–Th)/He thermochronometry using a radiation damage accumulation and annealing model. *Geochimica et Cosmochimica Acta*, **73(8)**, 2347‒2365, doi: 10.1016/j.gca.2009.01.015.

Foeken, J., Stuart, F.M., Dobson, K.J., Persano, C. & Vilbert, D. 2006. A diode laser system for heating minerals for (U-Th)/He chronometry. *Geochemistry, Geophysics, Geosystems*, **7(4),** doi: 10.1029/2005GC001190.

Forte, A.M., Quéré, S., Moucha, R., Simmons, N.A., Grand, S.P., Mitrovica, J.X., & Rowley, D.B. 2010. Joint seismic–geodynamic-mineral physical modelling of African geodynamics: A reconciliation of deep-mantle convection with surface geophysical constraints. *Earth and Planetary Science Letters*, **295(3–4)**, 329‒341, doi: 10.1016/j.epsl.2010.03.017.

Frizon de Lamotte, D., Fourdan, B., Leleu, S., Leparmentier, F. & Clarens, P. 2015. Style of rifting and the stages of Pangea breakup. *Tectonics*, **34(5)**, 1009‒1029, doi: doi.org/10.1002/2014TC003760.

Gadd, S.A. & Scrutton, R.A. 1997. An integrated thermomechanical model for transform continental margin evolution. *Geo-Marine Letters*, **17(1)**, 21‒30, doi: doi.org/10.1007/PL00007203.

Galbraith, R.F. 2005. *Statistics for fission track analysis*. Chapman and Hall/CRC, Florida. 240p.

Gallagher, K. 2012. Transdimensional inverse thermal history modeling for quantitative thermochronology. *Journal of Geophysical Research: Solid Earth*, **117(B2).**

Gallagher, K. (2017). QTQt User Guide v. 5.6.0 *(available by contacting the author).*

Gallagher, K. & Brown, R. 1999. Denudation and uplift at passive margins: The record on the Atlantic Margin of Southern Africa. *Philosophical Transactions: Mathematical, Physical and Engineering Sciences*, 835-859, doi: 10.1098/rsta.1999.0354.

Gallagher, K. 2016. Comment on 'A reporting protocol for thermochronologic modeling illustrated with data from the Grand Canyon' by Flowers, Farley and Ketcham. *Earth and Planetary Science Letters*, **441**, 211‒212, doi: 10.1016/j.epsl.2016.02.021.

Ganade, C.E., Cordani, U.G., Agbossoumounde, Y., Caby, R., Basei, M.A., Weinberg, R.F. & Sato, K. 2016. Tightening-up NE Brazil and NW Africa connections: New U–Pb/Lu–Hf zircon data of a complete plate tectonic cycle in the Dahomey belt of the West Gondwana Orogen in Togo and Benin. *Precambrian Research*, **276**, 24‒42, doi: 10.1016/j.precamres.2016.01.032.

Gautheron, C., Barbarand, J. *et al*. 2013. Chemical influence on α-recoil damage annealing in apatite: Implications for (U–Th)/He dating. *Chemical Geology*, **351**, 257–267, doi: 10.1016/j.chemgeo.2013.05.027.

Gautheron, C., Tassan-Got, L., Barbarand, J. & Pagel, M. 2009. Effect of alpha-damage annealing on apatite (U–Th)/He thermochronology. *Chemical Geology*, **266(3–4)**, 157–170, doi: 10.1016/j.chemgeo.2009.06.001.

Gerin, C., Gautheron, C. *et al*. 2017. Influence of vacancy damage on He diffusion in apatite, investigated at atomic to mineralogical scales. *Geochimica et Cosmochimica Acta*, **197**, 87–103, doi: 10.1016/j.gca.2016.10.018.

Gilchrist, A.R. & Summerfield, M.A. 1990. Differential denudation and flexural isostasy in formation of rifted-margin upwarps. *Nature*, **346(6286)**, 739–742, doi: 10.1038/346739a0.

Glodji, L.A., Bascou, J., Yessoufou, S., Ménot, R.P. & Villaros, A. 2014. Relationships between deformation and magmatism in the Pan-African Kandi Shear Zone: Microstructural and AMS studies of Ediacaran granitoid intrusions in central Bénin (West Africa). *Journal of African Earth Sciences*, **97**, 143–160, doi: 10.1016/j.jafrearsci.2014.04.012.

Grimaud, J.L., Chardon, D. & Beauvais, A. 2014. Very long-term incision dynamics of big rivers. *Earth and Planetary Science Letters*, **405**, 74–84, doi: 10.1016/j.epsl.2014.08.021.

Grimaud, J.L., Chardon, D., Metelka, V., Beauvais, A. & Bamba, O. 2015. Neogene cratonic erosion fluxes and landform evolution processes from regional regolith mapping (Burkina Faso, West Africa). *Geomorphology*, **241**, 315–330, doi: 10.1016/j.geomorph.2015.04.006.

Grimaud, J.L., Rouby, D., Chardon, D. & Beauvais, A. 2018. Cenozoic sediment budget of West Africa and the Niger delta. *Basin Research*, **30**, 169–186, doi:10.1111/bre.12248.

Guiraud, R. & Alidou, S. 1981. La faille de Kandi (Bénin), témoin du rejeu fini-crétacé d'un accident majeur à l'échelle de la plaque africaine. *Comptes Rendus Académie des Sciences. Paris, France*, **293**, 779–782.

Guiraud, M., Buta-Neto, A. & Quesne, D. 2010. Segmentation and differential post-rift uplift at the Angola margin as recorded by the transform-rifted Benguela and oblique-to-orthogonal-rifted Kwanza basins. *Marine and Petroleum Geology*, **27(5)**, 1040–1068, doi: 10.1016/j.marpetgeo.2010.01.017.

Guiraud, R. & Maurin, J.C. 1992. Early Cretaceous rifts of Western and Central Africa: an overview. *Tectonophysics*, **213(1-2)**, 153–168, doi: 10.1016/0040-1951(92)90256-6.

Guiraud, R., Bosworth, W., Thierry, J. & Delplanque, A. 2005. Phanerozoic geological evolution of Northern and Central Africa: an overview. *Journal of African Earth Sciences*, **43(1)**, 83‒143, doi: 10.1016/j.jafrearsci.2005.07.017.

Gunnell, Y. 2003. Radiometric ages of laterites and constraints on long-term denudation rates in West Africa: *Geology*, **31**, 131‒134, doi: 10.1130/0091-7613(2003)031<0131:RAOLAC>2.0.CO;2

Heine, C. & Brune, S. 2014. Oblique rifting of the Equatorial Atlantic: why there is no Saharan Atlantic Ocean. *Geology*, **42(3)**, 211‒214, doi: 10.1130/G35082.1.

Heine, C. Zoethout, J. & Müller, R.D. 2013. Kinematics of the South Atlantic rift. *Solid Earth*, **4**, 215‒253, doi: 10.5194/se-4-215-2013

Hurford, A.J. & Green, P.F. 1983. The zeta age calibration of fission-track dating. *Chemical Geology*, **41**, 285‒317, doi: 10.1016/S0009-2541(83)80026-6.

Jourdan, F., Marzoli, A. *et al*. (2009). ^{40}Ar/^{39}Ar ages of CAMP in North America: implications for the Triassic–Jurassic boundary and the ^{40}K decay constant bias. *Lithos*, **110(1–4)**, 167‒180, doi: 10.1016/j.lithos.2008.12.011.

Kaki, C., d'Almeida, G.A.F., Yalo, N. & Amelina, S. 2013. Geology and Petroleum Systems of the Offshore Benin Basin (Benin). *Oil and Gas Science and Technology–Revue d'IFP Energies nouvelles*, **68(2)**, 363‒381, doi: 10.2516/ogst/2012038.

Kalsbeek, F., Affaton, P., Ekwueme, B., Frei, R. & Thrane, K. 2012. Geochronology of granitoid and metasedimentary rocks from Togo and Benin, West Africa: Comparisons with NE Brazil. *Precambrian Research*, **196**, 218‒233, doi: 10.1016/j.precamres.2011.12.006.

Ketcham, R.A. 2005. The role of crystallographic angle in characterizing and modeling apatite fission-track length data. Radiation measurements, **39(6)**, 595‒601, doi: 10.1016/j.radmeas.2004.07.008.

Ketcham, R.A., Carter, A., Donelick, R.A., Barbarand, J., & Hurford, A.J. 2007. Improved modeling of fission-track annealing in apatite. *American Mineralogist*, **92(5-6)**, 799‒810, doi: 10.2138/am.2007.2281.

Knight, K.B., Nomade, S., Renne, P.R., Marzoli, A., Bertrand, H. & Youbi, N. 2004. The Central Atlantic Magmatic Province at the Triassic–Jurassic boundary: paleomagnetic and ^{40}Ar/^{39}Ar evidence from Morocco for brief, episodic volcanism. *Earth and Planetary Science Letters*, **228(1)**, 143‒160, doi: 10.1016/j.epsl.2004.09.022.

Konaté, M., Guiraud, M., Lang, J. & Yahaya, M. 2003. Sedimentation in the Kandi extensional basin (Benin and Niger): fluvial and marine deposits related to the Late Ordovician deglaciation in

West Africa. *Journal of African Earth Sciences*, **36(3)**, 185–206, doi: 10.1016/S0899-5362(03)00026-5.

Labails, C., Olivet, J.L., Aslanian, D. & Roest, W.R. 2010. An alternative early opening scenario for the Central Atlantic Ocean. *Earth and Planetary Science Letters*, **297(3-4)**, 355–368, doi: 10.1016/j.epsl.2010.06.024.

Lang, J., Kogbe, C. *et al*. (1990). The continental terminal in West Africa. *Journal of African Earth Sciences (and the Middle East)*, **10(1-2)**, 79–99, doi: 10.1016/0899-5362(90)90048-J.

Leleu, S., Hartley, A.J., van Oosterhout, C., Kennan, L., Ruckwied, K. & Gerdes, K. 2016. Structural, stratigraphic and sedimentological characterisation of a wide rift system: The Triassic rift system of the Central Atlantic Domain. *Earth-science reviews*, **158**, 89–124, doi: 10.1016/j.earscirev.2016.03.008.

Lesquer, A., Takherist, D., Dautria, J.M. & Hadiouche, O. 1990. Geophysical and petrological evidence for the presence of an "anomalous" upper mantle beneath the Sahara basins (Algeria). *Earth and Planetary Science Letters*, **96(3-4)**, 407–418, doi: 10.1016/0012-821X(90)90016-Q.

Liégeois, J.P., Sauvage, J.F. & Black, R. 1991. The Permo-Jurassic alkaline province of Tadhak, Mali: geology, geochronology and tectonic significance. *Lithos*, **27(2)**, 95–105.

Liégeois, J., Benhallou, A., Azzouni-Sekkal, A., Yahiaoui, R., & Bonin, B. 2005. The Hoggar swell and volcanism: reactivation of the Precambrian Tuareg shield during Alpine convergence and West African Cenozoic volcanism. *In:* Foulger, G.R., Natland, J.H., Presnall, D.C. & Anderson, D.L. (eds) *Plates, plumes and paradigms.* Special Papers - Geological Society of America, **388**, 379–400, doi: 10.1130/0-8137-2388-4.379.

Łuszczak, K., Persano, C., Braun, J. & Stuart, F.M. 2017. How local crustal thermal properties influence the amount of denudation derived from low-temperature thermochronometry. *Geology*, **45(9)**, 779–782, doi: 10.1130/G39036.1.

MacGregor, D.S., Robinson, J. & Spear, G. 2003. Play fairways of the Gulf of Guinea transform margin. *In:* Arthur, T., MacGregor, D.S. & Cameron, N.R. (eds) *Petroleum Geology of Africa: New Themes and Developing Technologies.* Geological Society, London, Special Publications, **207(1)**, 131–150, doi: 10.1144/GSL.SP.2003.207.7.

Mascle, J., Mougenot, D., Blarez, E., Marinho, M. & Virlogeux, P. 1987. African transform continental margins: Examples from Guinea, the Ivory Coast and Mozambique. *Geological Journal*, **22(S2)**, 537–561, doi: 10.1002/gj.3350220632.

Moody, R.T.J. & Sutcliffe, P.J.C. 1991. The Cretaceous deposits of the Iullemmeden basin of Niger, central West Africa. *Cretaceous Research,* **12(2)**, 137–157, doi: 10.1016/S0195-6671(05)80021-7.

Moulin, M., Aslanian, D. & Unternehr, P. 2010. A new starting point for the South and Equatorial Atlantic Ocean. *Earth-Science Reviews*, **98(1)**, 1–37, doi: 10.1016/j.earscirev.2009.08.001.

Nemčok, M., Henk, A., Allen, R., Sikora, P.J. & Stuart, C. 2013. Continental breakup along strike-slip fault zones; observations from the Equatorial Atlantic. In: Mohriak, W.U., Danforth, A., Post, P.J., Brown, D.E., Tari, G.C., Nemčok, M. & Sinha, S.T. (eds) *Conjugate Divergent Margins*. Geological Society, London, Special Publications, **369(1)**, 537–556, doi: 10.1144/SP369.8.

Peulvast, J.P., Bétard, F. & Lageat, Y. 2009. Long-term landscape evolution and denudation rates in shield and platform areas: a morphostratigraphic approach. *Géomorphologie: relief, processus, environnement,* **15(2)**, 95–108, doi: 10.4000/geomorphologie.7540.

Rahaman, M.A., Van Breemen, O., Bowden, P. & Bennett, J.N. 1984. Age migrations of anorogenic ring complexes in Northern Nigeria. *The Journal of Geology*, **92(2)**, 173–184, doi: 10.1086/628847.

Reiners, P.W. & Farley, K.A. 2001. Influence of crystal size on apatite (U–Th)/He thermochronology: an example from the Bighorn Mountains, Wyoming. *Earth and Planetary Science Letters*, **188(3)**, 413–420, doi: 10.1016/S0012-821X(01)00341-7.

Rouby, D., Braun, J., Robin, C., Dauteuil, O. & Deschamps, F. 2013. Long-term stratigraphic evolution of Atlantic-type passive margins: A numerical approach of interactions between surface processes, flexural isostasy and 3D thermal subsidence. *Tectonophysics*, **604**, 83–103, doi: 10.1016/j.tecto.2013.02.003.

Rougier, S., Missenard, Y. *et al*. 2013. Eocene exhumation of the Tuareg Shield (Sahara Desert, Africa). *Geology,* **41(5)**, 615–618, doi: 10.1130/G33731.1.

Soares, P.C., Assine, M.L. & Rabelo, L. 1998. The Pantanal Basin: recent tectonics, relationships to the Transbrasiliano Lineament. *Anais IX Simpósio Brasileiro de Sensoriamento Remoto,* 459–469.

Shuster, D.L., Flowers, R.M. & Farley, K.A. 2006. The influence of natural radiation damage on helium diffusion kinetics in apatite. *Earth and Planetary Science Letters*, **249(3)**, 148–161, 10.1016/j.epsl.2006.07.028.

Thieblemont., D. (ed) *et al.* (2016) Geological Map of Africa at 1:10,000,000 scale, CGMW-BRGM.

Todd, B.J. & Keen, C.E. 1989. Temperature effects and their geological consequences at transform margins. *Canadian Journal of Earth Sciences*, **26(12)**, 2591–2603, doi: 10.1139/e89-221.

Turcotte, D.L. & Schubert, G. (eds) 2002. *Geodynamics*. Cambridge, UK, Cambridge University Press, 456 p. doi: 10 .1017 /CBO9780511807442.

van Balen, R.T., van der Beek, P.A. & Cloetingh, S.A.P.L. 1995. The effect of rift shoulder erosion on stratal patterns at passive margins: implications for sequence stratigraphy. *Earth and Planetary Science Letters*, **134(3–4)**, 527–544, doi: 10.1016/0012-821X(95)98955-L.

van der Beek, P., Andriessen, P. & Cloetingh, S. 1995. Morphotectonic evolution of rifted continental margins: Inferences from a coupled tectonic-surface processes. *Tectonics*, **14(2)**, 406–421, doi: 10.1029/94TC02445.

van der Beek, P., Summerfield, M.A., Braun, J., Brown, R.W. & Fleming, A. 2002. Modeling postbreakup landscape development and denudational history across the southeast African (Drakensberg Escarpment) margin. *Journal of Geophysical Research: Solid Earth*, **107(B12)**, doi: 10.1029/2001JB000744.

Withjack, M.O., Schlische, R.W. & Olsen, P.E. 1998. Diachronous rifting, drifting, and inversion on the passive margin of central eastern North America: an analog for other passive margins. *American Association of Petroleum Geologists (AAPG) bulletin*, **82(5)**, 817–835.

Wolf, R.A., Farley, K.A. & Kass, D.M. 1998. Modeling of the temperature sensitivity of the apatite (U–Th)/He thermochronometer. *Chemical Geology*, **148(1)**, 105–114, doi: 10.1016/S0009-2541(98)00024-2.

Ye, J., Chardon, D., Rouby, D., Guillocheau, F., Dall'Asta, M., Ferry, J.N. & Broucke, O. 2017. Paleogeographic and structural evolution of northwestern Africa and its Atlantic margins since the early Mesozoic. *Geosphere*, **13**, 1254–1284, doi:10.1130/GES01426.1.

Zhao, D. 2007. Seismic images under 60 hotspots: search for mantle plumes. *Gondwana Research*, **12(4)**, 335–355, doi: 10.1016/j.gr.2007.03.001.

Table 1: *Apatite fission-track data*

Sample	Lon. (°)	Lat. (°)	Elev. (m)	Lithology	Strat. Age	ρ_s[a] (x10^{5}cm^{-2})	ρ_i[a] (x10^{5}cm^{-2})	ρ_d[a] (x10^{5}cm^{-2})	AFT Age[b] (Ma)	# Xtls[c]	MTL[d] (μm)	MTL St. Dev.	# L[c]	P (χ^2)[e]	Disp.[f]	D_{par} (μm)
BN01	2.09	7.40	160	Granitoid	Proterozoic	7.8	15.3	16.2	125 ± 11	26	13.8 ± 0.1	0.93	49	0.00	34%	1.78 ± 0.13
BN02	2.19	7.62	144	Gneiss	Proterozoic	10.2	18.3	15.9	132 ± 7	22	14.0 ± 0.1	0.99	100	0.00	19%	1.78 ± 0.12
BN03	2.50	8.05	197	Granitoid	Proterozoic	6.1	14.1	15.8	107 ± 7	22	14.4 ± 0.1	0.83	106	0.00	25%	1.75 ± 0.13
BN04	2.61	8.75	302	Granitoid	Proterozoic	5.8	13.3	15.7	106 ± 5	20	14.1 ± 0.1	1.01	104	0.16	9%	1.66 ± 0.11
BN05	2.55	9.19	374	Granitoid	Proterozoic	7.8	16.9	15.9	113 ± 5	20	14.1 ± 0.1	0.89	105	0.01	14%	1.72 ± 0.09
BN06	3.19	11.68	238	Sandstone	Ordovician-Silurian	10.2	19.1	15.3	130 ± 11	15	13.8 ± 0.3	0.91	19	0.10	21%	1.87 ± 0.14
BN07	2.90	11.14	298	Gneiss	Neoproterozoic	18.6	11.2	15.2	386 ± 16	22	13.9 ± 0.3	0.94	134	0.30	7%	2.04 ± 0.12
BN08	2.81	10.80	347	Sandstone	Cambrian-Silurian	3.9	4.3	15.0	219 ± 38	15	13.4 ± 0.3	1.07	22	0.00	61%	2.00 ± 0.27
BN09	2.73	10.56	351	Gneiss	Proterozoic	28.0	18.9	14.8	338 ± 13	20	13.3 ± 0.1	1.01	151	0.00	13%	1.86 ± 0.12
BN10	2.72	10.37	345	Gneiss	Proterozoic	55.6	32.7	14.7	380 ± 14	20	13.5 ± 0.1	0.95	249	0.00	14%	2.02 ± 0.13
BN11	2.60	9.77	346	Granitoid	Proterozoic	6.7	8.2	14.4	182 ± 10	20	13.9 ± 0.2	1.10	102	0.00	15%	1.73 ± 0.08
BN12	2.30	9.77	338	Migmatite	Proterozoic	26.4	28.6	14.3	203 ± 8	20	14.2 ± 0.1	0.96	151	0.00	15%	1.90 ± 0.11
BN13	1.51	10.01	397	Granitiod	Proterozoic	13.8	17.8	14	168 ± 7	20	13.8 ± 0.2	1.05	120	0.02	12%	1.69 ± 0.09
BN14	1.19	10.76	247	Sandstone	Lower Paleozoic	24.0	24.2	13.8	217 ± 33	8	13.2 ± 0.4	1.21	33	0.00	39%	1.81 ± 0.08
BN15	1.28	10.61	268	Sandstone	Lower Paleozoic	35.0	32.2	13.55	227 ± 15	8	13.7 ± 0.2	1.33	55	0.12	9%	1.78 ± 0.10
BN16	1.32	10.56	557	Sandstone	Lower Paleozoic	4.1	2.6	16.8	401 ± 45	3	13.8 ± 0.5	1.53	8	0.93	0%	1.88 ± 0.06
BN17	2.63	8.36	262	Gneiss	Proterozoic	4.8	9.2	13.4	109 ± 6	20	14.3 ± 0.2	0.95	98	0.16	11%	1.69 ± 0.11
BN18	1.82	7.06	203	Sandstone	Maastrichtian	3.3	9.1	16.3	112 ± 25	6	12.4 ± 0.7	1.32	8	0.05	35%	1.76 ± 0.16

a: ρ_i,ρ_s,ρ_d are track density of induced, spontaneous, dosimeter tracks.

b: AFT ages are central ages calculated with 1σ standard error, calculated using a $\zeta = 313.3 \pm 9.6$ for a standard IRMM540 glass.

c: #Xtls and #L are the number of crystals counted and the number of horizontal confined track lengths measured, respectively.

d: Mean track lengths with 1σ standard error are corrected for their orientation to the c-axis after Ketcham (2005).

e: P(χ^2) is p-value of the chi-sq age homogeneity test (Galbraith, 2005).

f: Dispersion is the standard deviation of the single-grain ages as a percentage of their central age.

Table 2: *Apatite (U-Th-Sm)/He data*

Sample	Grain #	^{4}He (ncc/g)	^{238}U (ppm)	^{235}U (ppm)	^{232}Th (ppm)	^{147}Sm (ppm)	eU^{a} (ppm)	T^{b}	L^{c} (µm)	W^{d} (µm)	R*^{e} (µm)	F_t^{f}	AHe Age^{g} (Ma)	Cor. AHe Age^{g} (Ma)
BN2	1	3.8E+05	22.3	0.16	28.4	*n.d.*	29.1	2	241	95	59.5	0.75	106.4 ± 12.2	141.8 ± 16.3
	2	8.9E+04	5.5	0.04	17.8		9.7	2	201	85	52.6	0.71	74.8 ± 10.3	105.8 ± 14.6
BN3	1	4.2E+04	3.1	0.02	8.5	*n.d.*	5.1	2	287	133	81.0	0.81	67.2 ± 8.3	82.9 ± 10.2
	2	1.3E+05	5.5	0.04	19.1	31.7	10.0	0	156	143	73.5	0.79	107.2 ± 12.8	135.8 ± 16.1
	3	2.3E+05	14.6	0.11	20.7	*n.d.*	19.5	2	269	128	77.5	0.81	94.9 ± 10.7	117.6 ± 13.2
	4	1.3E+05	8.3	0.06	19.4	26.6	12.9	1	187	144	78.0	0.80	79.6 ± 9.2	98.9 ± 11.4
	5	2.1E+05	11.5	0.08	30.5	31.3	18.7	1	190	144	78.3	0.80	90.3 ± 10.2	112.2 ± 12.7
	6	9.4E+04	5.9	0.04	29.6	29.3	12.9	0	117	124	60.8	0.74	60.0 ± 7.3	80.8 ± 9.9
	7	9.7E+04	5.2	0.04	13.3	17.2	8.3	1	162	156	79.0	0.81	95.5 ± 11.4	118.4 ± 14.2
	8	2.3E+05	10.6	0.08	50.9	59.7	22.6	1	216	131	75.4	0.79	83.4 ± 9.5	105.3 ± 11.9
	9	4.2E+04	3.6	0.03	7.4	23.5	5.3	1	174	122	67.7	0.78	65.3 ± 9.5	84.1 ± 12.3
	10	3.9E+05	12.6	0.09	46.8	21.6	23.7	1	146	123	64.9	0.76	135.7 ± 15.6	178.3 ± 20.5
	11	6.9E+04	8.7	0.06	28.9	*n.d.*	15.5	2	179	73	45.5	0.66	36.4 ± 5.0	55.2 ± 7.5
	12	2.2E+05	10.1	0.07	21.7	34.2	15.2	1	160	156	78.7	0.81	119.3 ± 13.7	147.8 ± 16.9
	13	3.0E+05	10.4	0.07	46.5	234.3	21.4	1	132	171	77.8	0.80	114.6 ± 13.0	143.4 ± 16.2
	14	8.4E+04	2.8	0.02	12.9	6.7	5.8	1	434	280	158.8	0.90	117.8 ± 13.3	130.7 ± 14.7
	15	1.1E+05	5.3	0.04	13.4	22.5	8.5	0	227	220	111.1	0.86	106.1 ± 11.9	123.0 ± 13.8
	16	4.4E+04	2.3	0.02	4.2	13.5	3.3	1	179	185	91.5	0.84	108.0 ± 14.3	129.3 ± 17.1
	17	3.2E+05	9.1	0.07	34.5	44.6	17.2	1	260	149	86.9	0.82	152.7 ± 17.2	185.9 ± 21.0
	18	3.7E+05	20.2	0.15	41.0	44.6	30.0	1	186	117	66.8	0.77	101.3 ± 11.5	131.0 ± 14.8
	19	2.3E+05	12.1	0.09	27.4	35.8	18.7	1	158	109	60.8	0.75	101.7 ± 12.1	135.7 ± 16.2
	20	1.9E+05	13.9	0.10	14.5	*n.d.*	17.4	2	241	124	74.0	0.80	91.2 ± 10.5	113.9 ± 13.1
	21	1.1E+05	4.9	0.04	20.2	5.6	9.7	1	241	223	114.3	0.86	96.2 ± 10.8	111.4 ± 12.5
	22	7.8E+04	4.3	0.03	11.1	4.9	6.9	1	191	156	83.1	0.82	91.9 ± 11.0	112.6 ± 13.5
BN4	1	7.7E+04	5.5	0.04	9.5	*n.d.*	7.8	2	180	100	58.7	0.74	80.8 ± 12.1	108.7 ± 16.2
	2	1.7E+05	10.8	0.08	11.9		13.7	2	206	123	71.0	0.79	103.1 ± 12.4	130.2 ± 15.6
	3	9.2E+04	6.0	0.04	4.7		7.1	2	450	186	115.6	0.87	105.6 ± 11.9	121.4 ± 13.7
BN5	1	3.8E+05	23.0	0.17	14.0	*n.d.*	26.4	2	374.0	91.0	60.8	0.76	117 ± 13.4	153.8 ± 17.6
	2	2.4E+05	8.0	0.06	4.7		9.2	2	314.0	199.0	113.3	0.87	213.4 ± 24.1	244.7 ± 27.6
	3	4.9E+04	2.8	0.02	0.6		3.0	2	297.0	242.0	129.0	0.89	135.9 ± 18.2	152.8 ± 20.4

Table 2: *Apatite (U-Th-Sm)/He data*

Sample	Grain #	^{4}He (ncc/g)	^{238}U (ppm)	^{235}U (ppm)	^{232}Th (ppm)	^{147}Sm (ppm)	eU[a] (ppm)	T[b]	L[c] (µm)	W[d] (µm)	R*[e] (µm)	F_t[f]	AHe Age[g] (Ma)	Cor. AHe Age[g] (Ma)
	4	3.7E+04	2.5	0.02	0.8	*n.d.*	2.7	2	500.0	268.0	158.5	0.91	112.2 ± 13.0	123.3 ± 14.2
	5	5.1E+04	3.2	0.02	1.9		3.7	2	403.0	275.0	153.8	0.91	114.3 ± 12.9	126.2 ± 14.3
	6	1.2E+05	5.7	0.04	3.6		6.6	2	318.0	252.0	135.4	0.89	143.3 ± 16.1	160.6 ± 18.0
BN7	1	7.7E+04	3.5	0.03	5.4	2.1	4.8	1	127.0	111.0	57.9	0.74	130.6 ± 23.5	176.1 ± 31.7
	2	8.3E+04	3.4	0.02	2.4	2.3	3.9	1	105.0	144.0	64.1	0.77	170.1 ± 33.0	220.2 ± 42.7
	3	2.5E+05	7.7	0.06	6.2	*n.d.*	9.2	2	183.0	119.0	67.4	0.78	220.4 ± 29.2	281.6 ± 37.3
	4	2.9E+05	8.8	0.06	8.5		10.8	2	125.0	68.0	40.1	0.63	220.4 ± 46.4	348.4 ± 73.3
	5	9.4E+04	3.6	0.03	5.5		5.0	2	128.0	115.0	59.5	0.75	153.5 ± 26.3	205.1 ± 35.1
	6	2.4E+05	5.2	0.04	31.5		12.6	1	194.0	194.0	97.0	0.84	153.2 ± 17.4	183.0 ± 20.8
	7	1.3E+05	5.7	0.04	7.3		7.4	1	116.0	73.0	41.6	0.64	141.6 ± 33.8	220.2 ± 52.6
	8	1.1E+05	3.7	0.03	4.9		4.9	2	169.0	131.0	70.8	0.79	175.8 ± 25.5	222.5 ± 32.3
	9	2.5E+05	10.7	0.08	14.0		14.1	2	173.0	67.0	42.1	0.65	145.5 ± 22.9	224.9 ± 35.5
	10	1.4E+05	6.1	0.04	12.4		9.0	2	125.0	83.0	46.7	0.68	127.2 ± 21.5	188.0 ± 31.9
	11	4.7E+04	2.0	0.01	2.9		2.7	2	127.0	86.0	48.2	0.69	140.9 ± 47.7	204.1 ± 69.2
	12	1.3E+05	4.5	0.03	2.7		5.1	1	129.0	93.0	51.3	0.72	200.2 ± 49.2	279.4 ± 68.7
	13	2.5E+05	7.7	0.06	7.3		9.5	2	133.0	108.0	57.6	0.74	211.3 ± 31.4	283.8 ± 42.4
BN9	1	2.6E+05	8.7	0.06	1.5	*n.d.*	9.1	2	250.0	132.0	78.3	0.82	227.5 ± 44.7	278.2 ± 54.6
	2	6.0E+05	11.7	0.08	2.3		12.3	2	270.0	103.0	64.9	0.78	390.1 ± 74.4	500.2 ± 95.4
BN10	1	6.2E+05	17.6	0.13	0.5	*n.d.*	17.8	2	339.0	216.0	122.9	0.88	280.5 ± 48.4	317.0 ± 54.7
	2	6.8E+05	18.8	0.14	0.9		19.1	2	333.0	193.0	112.2	0.87	286.9 ± 39.9	328.4 ± 45.7
	3	3.5E+05	12.9	0.09	0.5		13.1	2	365.0	185.0	110.7	0.87	214.2 ± 43.1	245.6 ± 49.4
BN11	1	3.6E+04	1.2	0.01	8.3	*n.d.*	3.2	2	290.0	216.0	118.0	0.87	92.8 ± 10.7	107.2 ± 12.4
	2	5.5E+04	2.6	0.02	7.8		4.4	2	380.0	241.0	137.2	0.89	101.8 ± 11.5	114.6 ± 12.9
	3	1.1E+05	1.8	0.01	2.4		2.3	2	453.0	256.0	149.7	0.90	386.4 ± 44.0	429.1 ± 48.9
	4	7.6E+04	1.8	0.01	6.5		3.3	2	185.0	118.0	67.1	0.77	187.3 ± 30.6	243.5 ± 39.7
	5	2.8E+04	1.9	0.01	3.2		2.6	2	300.0	179.0	103.4	0.85	85.9 ± 10.9	100.5 ± 12.7
	6	1.9E+05	13.8	0.10	23.1		19.4	2	277.0	115.0	71.4	0.79	82.4 ± 9.4	104.4 ± 11.9
BN12	1	8.1E+05	27.6	0.20	4.1		28.8	1	142.0	146.0	72.3	0.80	229.1 ± 29.3	285.3 ± 36.4
	2	6.3E+05	22.9	0.16	5.0		24.2	1	88.0	139.0	58.2	0.75	211.7 ± 32.7	280.5 ± 43.3
	3	4.1E+05	14.9	0.11	2.2	*n.d.*	15.5	2	313.0	184.0	106.7	0.87	215.4 ± 25.1	248.6 ± 29.0

Table 2: *Apatite (U-Th-Sm)/He data*

Sample	Grain #	^{4}He (ncc/g)	^{238}U (ppm)	^{235}U (ppm)	^{232}Th (ppm)	^{147}Sm (ppm)	eU^{a} (ppm)	T^{b}	L^{c} (µm)	W^{d} (µm)	R*^{e} (µm)	F_t ^{f}	AHe Age^{g} (Ma)	Cor. AHe Age^{g} (Ma)
	4	9.0E+05	31.9	0.23	4.6		33.2	2	276.0	157.0	91.7	0.84	220.8 ± 25.3	261.3 ± 30.0
	5	3.5E+05	16.5	0.12	2.3		17.2	2	233.0	125.0	73.9	0.81	167.5 ± 25.9	207.4 ± 32.1
	6	3.8E+04	2.4	0.02	0.8	*n.d.*	2.6	2	238.0	129.0	76.1	0.81	119.1 ± 46.9	146.8 ± 57.8
BN14	1	1.0E+06	38.6	0.28	3.0	*n.d.*	39.6	1	304.0	280.0	143.8	0.90	209.7 ± 23.8	232.7 ± 26.5
	2	5.2E+05	23.7	0.17	3.4		24.7	1	153.0	150.0	75.5	0.81	173.0 ± 22.2	213.3 ± 27.4
BN17	1	1.1E+05	9.1	0.07	1.6	*n.d.*	9.5	2	242	129.0	76.4	0.81	91.6 ± 15.5	112.6 ± 19.0
	2	9.2E+03	3.2	0.02	1.0		3.4	2	229	186.0	99.2	0.86	22.1 ± 3.3	25.8 ± 3.9
	3	2.5E+04	5.4	0.04	1.2		5.7	2	239	142.0	82.1	0.83	36.2 ± 6.6	43.9 ± 8.0
	4	2.5E+04	5.7	0.04	4.0		6.7	2	143	90.0	51.3	0.72	30.7 ± 8.8.	42.9 ± 12.3
	5	1.3E+04	3.7	0.03	3.7		4.6	2	164	98.0	56.6	0.74	22.8 ± 5.6	30.8 ± 7.6
	6	1.2E+05	9.9	0.07	2.2		10.5	2	218	112.0	66.8	0.79	92.4 ± 16.1	117.5 ± 20.5
BN18	1	1.9E+05	15.5	0.11	12.7	*n.d.*	18.6	2	143.0	54.0	34.1	0.57	83.7 ± 21.7	146.8 ± 38.1
	2	3.4E+05	6.0	0.04	11.1		8.6	2	177.0	160.0	82.6	0.82	313.9 ± 37.2	383.9 ± 45.4
	3	1.1E+06	30.1	0.22	19.8		35.0	2	168.0	52.0	33.8	0.57	263.9 ± 43.5	464.1 ± 76.5
	4	3.4E+04	2.4	0.02	5.8		3.8	2	132.0	95.0	52.4	0.71	73.0 ± 21.0	102.9 ± 29.6

a: [eU] = [U]+(0.235*[Th])

b: T = Number of crystal terminations.

c: L = crystal length

d: W = crystal width

e: R* = spherical equivalent radius.

f: Ft is the correction factor to account for alpha-ejection from the outer rim of the apatite crystal (Farley et al., 1996).

g: Estimated uncertainty includes error propagated from U, Th, Sm and He measurement, plus an additional 10% which is the standard deviation (reproducibility) of repeat analysis of Durango apatite standards.

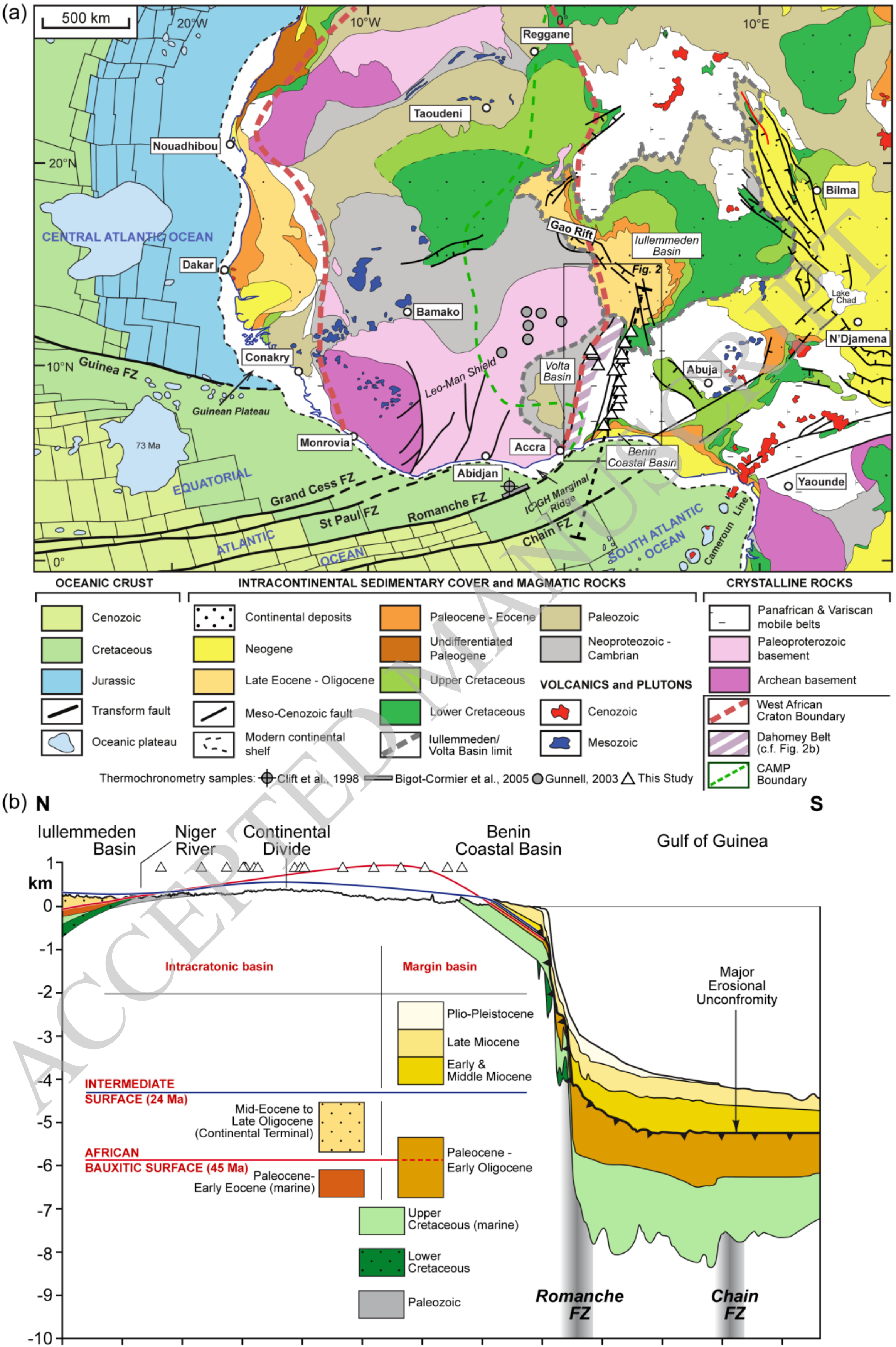
(a)
500 km
20°W
10°W
0°
10°E
20°N
10°N
0°
Reggane
Taoudeni
Nouadhibou
Dakar
Bamako
Conakry
Monrovia
Abidjan
Accra
Abuja
Bilma
N'Djamena
Yaounde
Lake Chad
Gao Rift
Iullemmeden Basin
Fig. 2
Volta Basin
Benin Coastal Basin
Leo-Man Shield
CENTRAL ATLANTIC OCEAN
Guinea FZ
Guinean Plateau
73 Ma
EQUATORIAL
ATLANTIC
OCEAN
Grand Cess FZ
St Paul FZ
Romanche FZ
IC-GH Marginal Ridge
Chain FZ
SOUTH ATLANTIC OCEAN
Cameroun Line
OCEANIC CRUST
Cenozoic
Cretaceous
Jurassic
Transform fault
Oceanic plateau
INTRACONTINENTAL SEDIMENTARY COVER and MAGMATIC ROCKS
Continental deposits
Neogene
Late Eocene - Oligocene
Meso-Cenozoic fault
Modern continental shelf
Paleocene - Eocene
Undifferentiated Paleogene
Upper Cretaceous
Lower Cretaceous
Iullemmeden/ Volta Basin limit
Paleozoic
Neoproterozoic - Cambrian
VOLCANICS and PLUTONS
Cenozoic
Mesozoic
CRYSTALLINE ROCKS
Panafrican & Variscan mobile belts
Paleoproterozoic basement
Archean basement
West African Craton Boundary
Dahomey Belt (c.f. Fig. 2b)
CAMP Boundary
Thermochronometry samples: Clift et al., 1998 Bigot-Cormier et al., 2005 Gunnell, 2003 This Study
(b) N
S
Iullemmeden Basin
Niger River
Continental Divide
Benin Coastal Basin
Gulf of Guinea
km
1
0
-1
-2
-3
-4
-5
-6
-7
-8
-9
-10
Intracratonic basin
Margin basin
Plio-Pleistocene
Late Miocene
Early & Middle Miocene
INTERMEDIATE SURFACE (24 Ma)
Mid-Eocene to Late Oligocene (Continental Terminal)
AFRICAN BAUXITIC SURFACE (45 Ma)
Paleocene- Early Eocene (marine)
Paleocene - Early Oligocene
Upper Cretaceous (marine)
Lower Cretaceous
Paleozoic
Major Erosional Unconfromity
Romanche FZ
Chain FZ
0 km
200
400
600
800
1000
1200

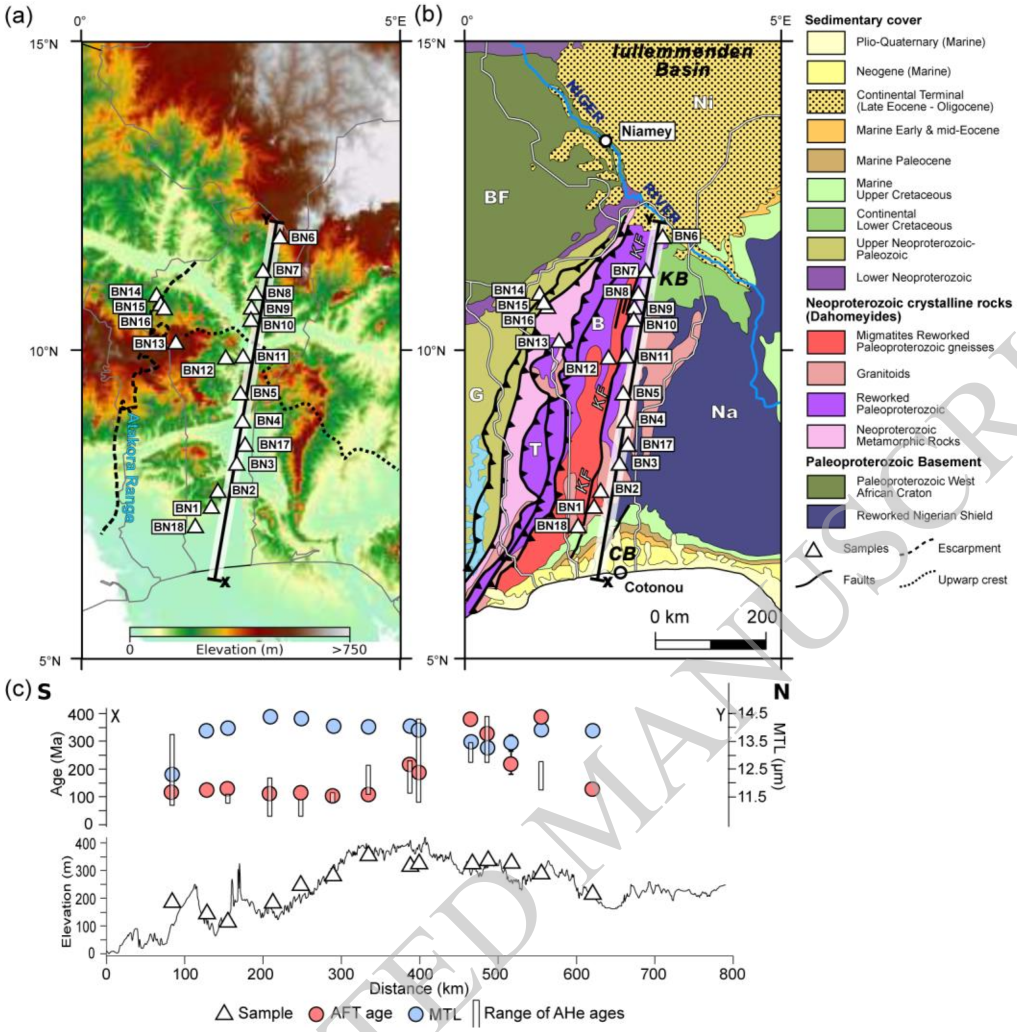
(a)
(b)
(c)
0°
5°E
15°N
10°N
5°N
BN1
BN2
BN3
BN4
BN5
BN6
BN7
BN8
BN9
BN10
BN11
BN12
BN13
BN14
BN15
BN16
BN17
BN18
Atakora Range
0
Elevation (m)
>750
Iullemmenden Basin
Ni
NIGER RIVER
Niamey
BF
KB
B
G
T
KF
Na
CB
Cotonou
0 km
200
Sedimentary cover
Plio-Quaternary (Marine)
Neogene (Marine)
Continental Terminal (Late Eocene - Oligocene)
Marine Early & mid-Eocene
Marine Paleocene
Marine Upper Cretaceous
Continental Lower Cretaceous
Upper Neoproterozoic-Paleozoic
Lower Neoproterozoic
Neoproterozoic crystalline rocks (Dahomeyides)
Migmatites Reworked Paleoproterozoic gneisses
Granitoids
Reworked Paleoproterozoic
Neoproterozoic Metamorphic Rocks
Paleoproterozoic Basement
Paleoproterozoic West African Craton
Reworked Nigerian Shield
Samples
Escarpment
Faults
Upwarp crest
S
N
X
Y
Age (Ma)
0
100
200
300
400
MTL (µm)
11.5
12.5
13.5
14.5
Elevation (m)
Distance (km)
0
100
200
300
400
500
600
700
800
Sample
AFT age
MTL
Range of AHe ages

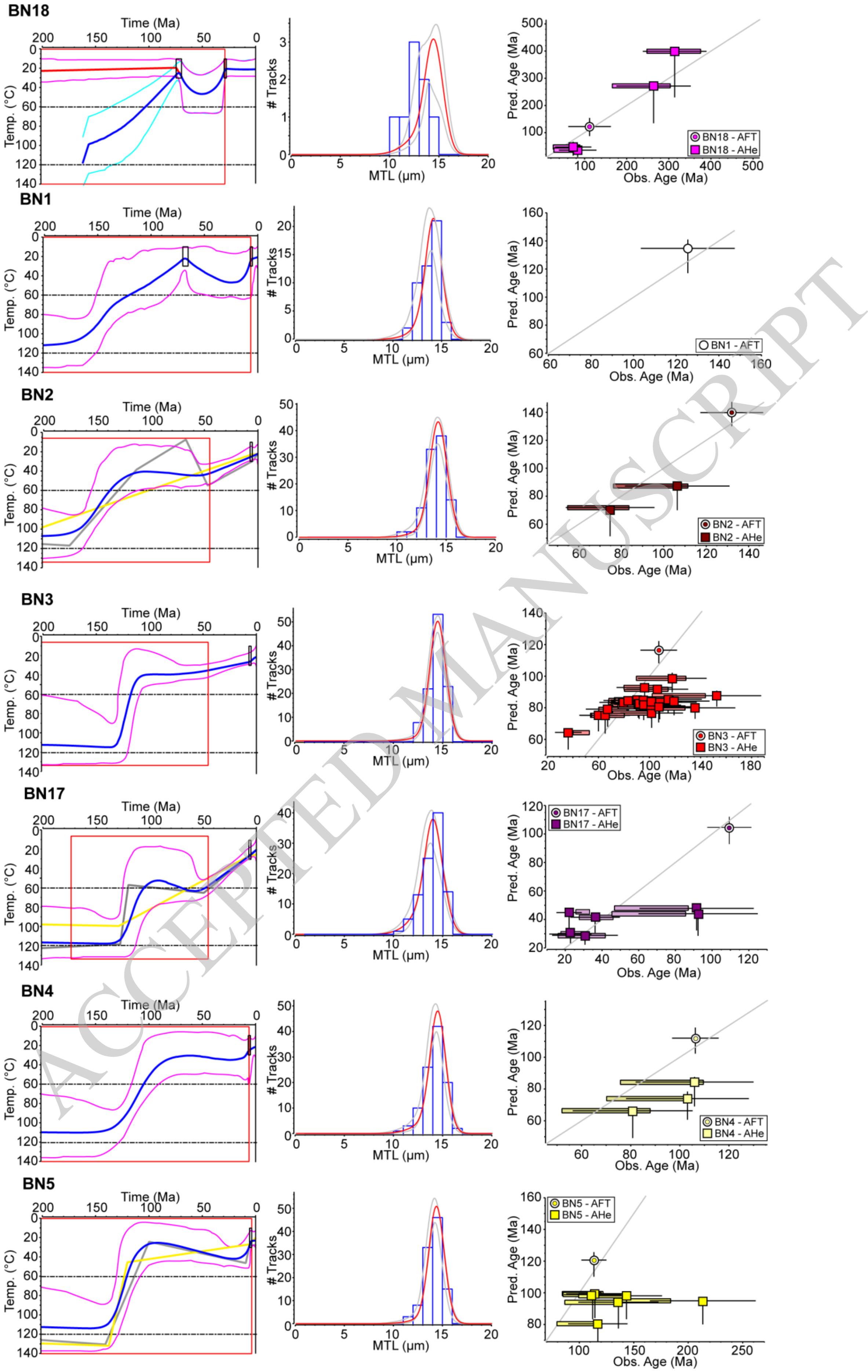
BN18
BN1
BN2
BN3
BN17
BN4
BN5
Time (Ma)
200
150
100
50
0
Temp. (°C)
20
40
60
80
100
120
140
Tracks
MTL (µm)
5
10
15
20
Pred. Age (Ma)
Obs. Age (Ma)
BN18 - AFT
BN18 - AHe
BN1 - AFT
BN2 - AFT
BN2 - AHe
BN3 - AFT
BN3 - AHe
BN17 - AFT
BN17 - AHe
BN4 - AFT
BN4 - AHe
BN5 - AFT
BN5 - AHe

BN10

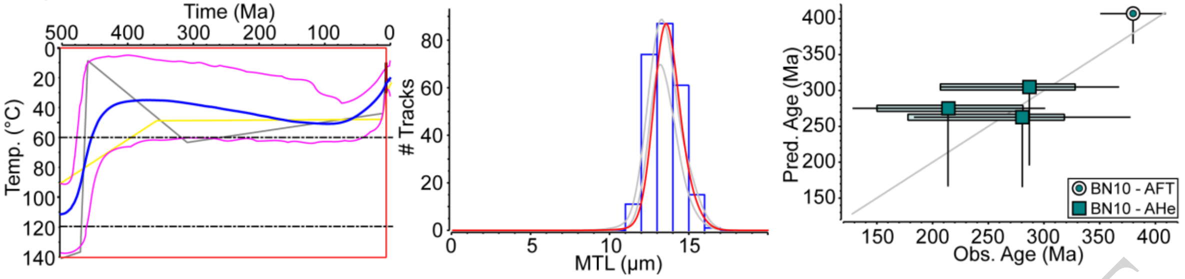

BN11

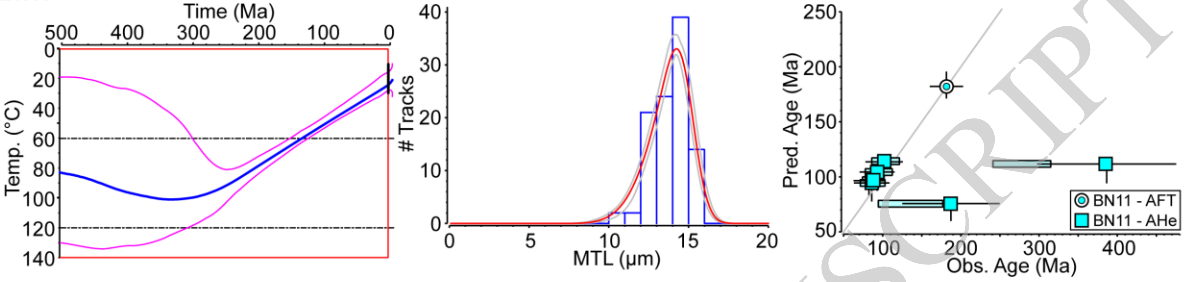

BN12

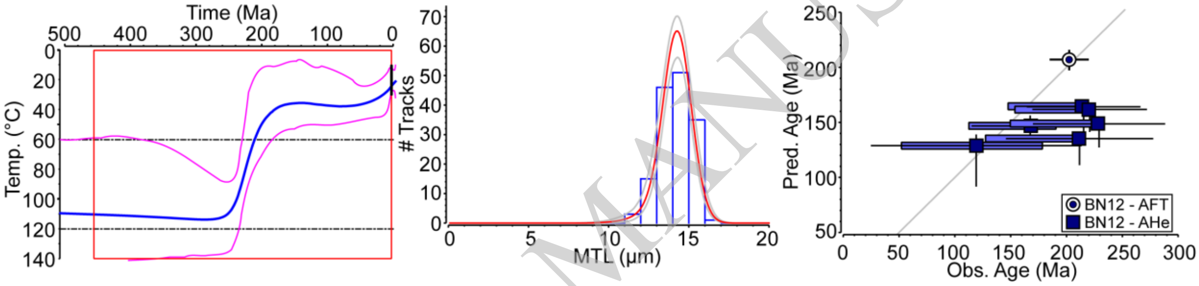

BN9

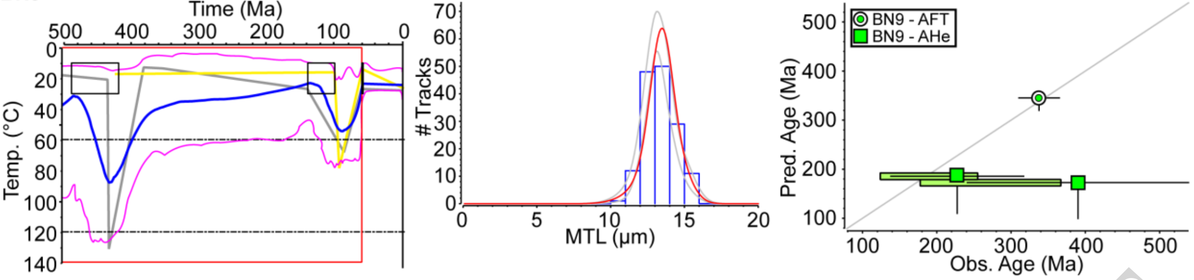

BN8

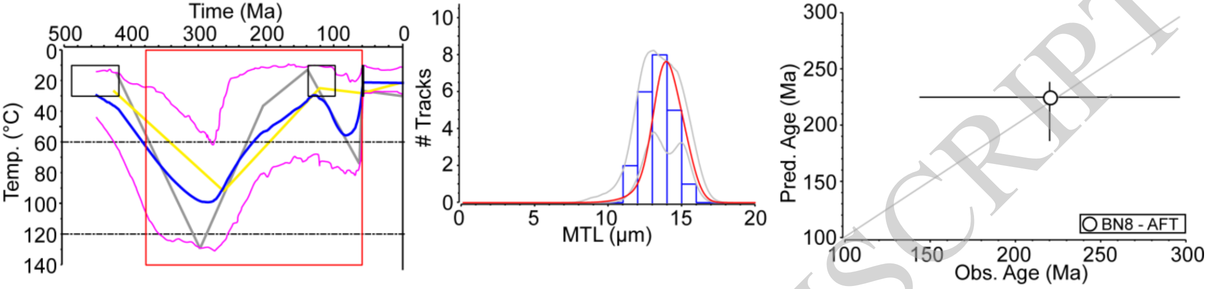

BN7

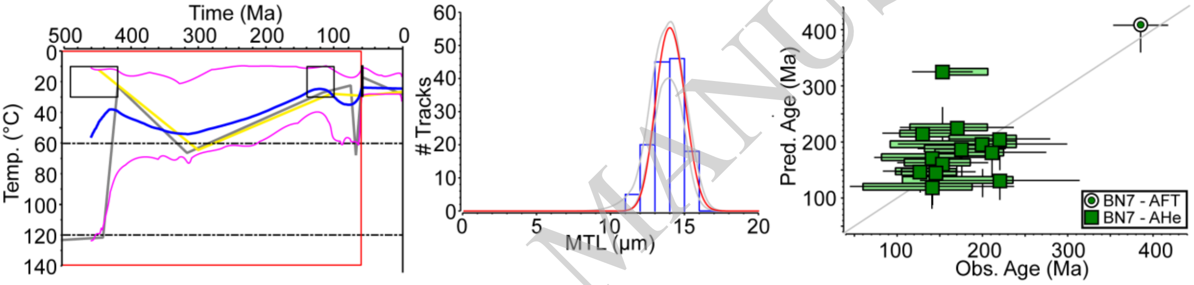

BN6

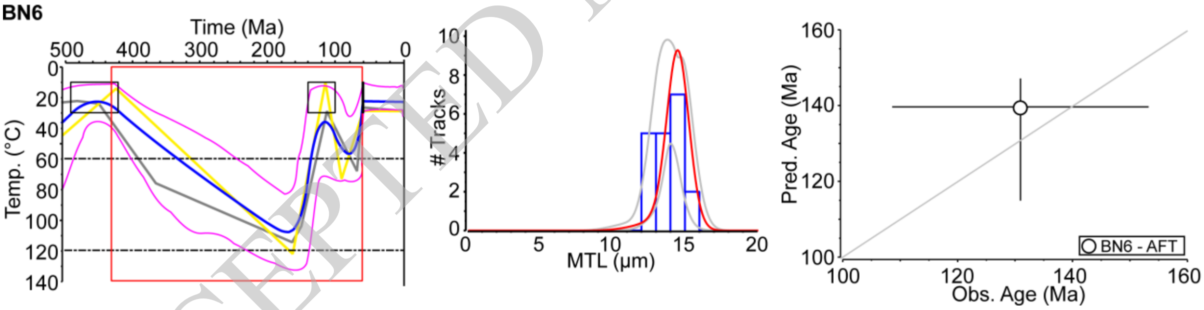

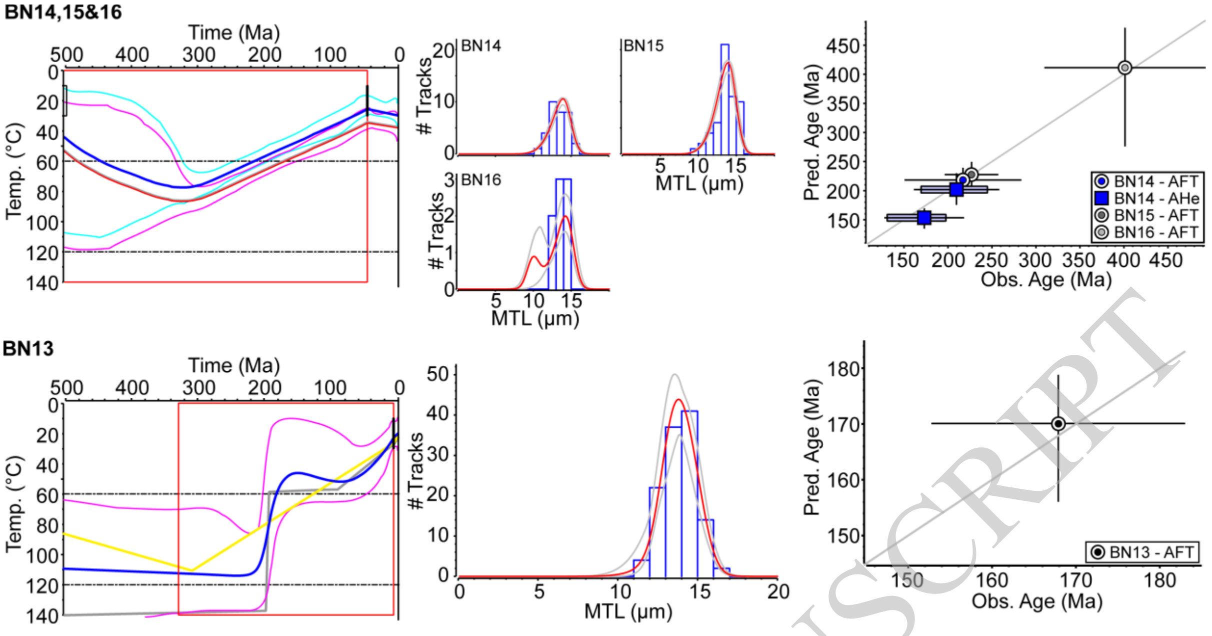
BN14,15&16
Time (Ma)
500 400 300 200 100 0
Temp. (°C)
0 20 40 60 80 100 120 140
BN14
BN15
BN16
Tracks
MTL (µm)
5 10 15
Pred. Age (Ma)
Obs. Age (Ma)
150 200 250 300 350 400 450
BN14 - AFT
BN14 - AHe
BN15 - AFT
BN16 - AFT
BN13
0 5 10 15 20
0 10 20 30 40 50
150 160 170 180
BN13 - AFT

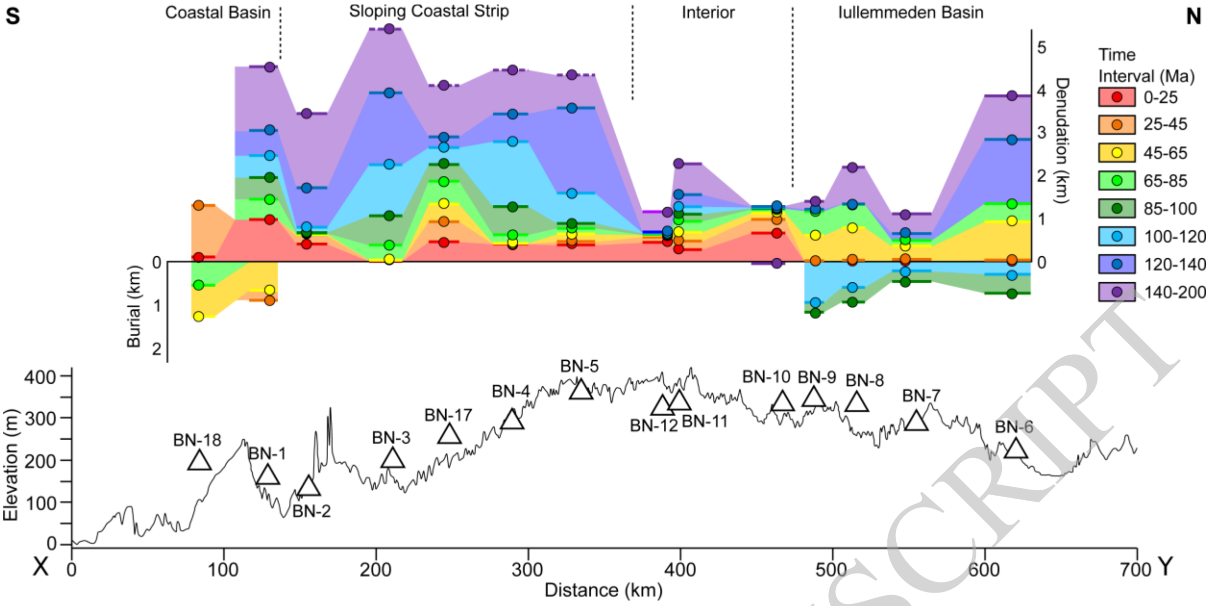
S
Coastal Basin
Sloping Coastal Strip
Interior
Iullemmeden Basin
N
Time Interval (Ma)
0-25
25-45
45-65
65-85
85-100
100-120
120-140
140-200
Denudation (km)
0
1
2
3
4
5
Burial (km)
0
1
2
Elevation (m)
0
100
200
300
400
BN-18
BN-1
BN-2
BN-3
BN-17
BN-4
BN-5
BN-12
BN-11
BN-10
BN-9
BN-8
BN-7
BN-6
X
Y
0
100
200
300
400
500
600
700
Distance (km)